Cross-Sectional Scanning Tunneling Microscopy

Edward T. Yu

Department of Electrical and Computer Engineering, University of California at San Diego, La Jolla, California 92093-0407

Received September 23, 1996 (Revised Manuscript Received March 24, 1997)

Contents

Edward Yu is Associate Professor in the Department of Electrical and Computer Engineering at the University of California, San Diego. He received his A.B. (summa cum laude) and A.M. degrees in Physics from Harvard University in 1986, and his Ph.D. degree in Applied Physics from the California Institute of Technology in 1991. While at Caltech he was the recipient of a National Science Foundation Graduate Fellowship and an AT&T Bell Laboratories Ph.D. Scholarship. He joined the faculty of UCSD in September 1992 following a one-year postdoctoral appointment at the IBM Thomas J. Watson Research Center in Yorktown Heights, NY. Professor Yu's research interests are in the area of semiconductor materials and devices, including atomic-scale characterization of semiconductor heterostructures and devices; fundamental properties and applications of novel heterojunction material systems; and techniques for the fabrication and characterization of nanometer-scale semiconductor device structures. Recent activities in his research group at UCSD have included extensive studies using cross-sectional scanning tunneling microscopy of atomic-scale properties, and their relation to epitaxial growth conditions and device performance, of a wide range of III–V compound semiconductor heterostructures. Professor Yu has been the recipient of an Office of Naval Research Young Investigator Award, and Alfred P. Sloan Research Fellowship, and a National Science Foundation CAREER Award.

I. Introduction

Since its invention in the early 1980, scanning tunneling microscopy[1−4] (STM) and techniques such as atomic force microscopy[5] (AFM) that have evolved from it have become tools of paramount importance in fundamental studies of surfaces. In addition, increasing effort has been directed towards the use of STM and related techniques to address problems of technological interest, particularly in the area of semiconductor materials and devices. The extremely high spatial resolution afforded by these techniques has led naturally to their application to a wide range of scientific and technological problems in semiconductor device physics. Indeed, their growing importance in semiconductor science and technology is a natural consequence of the desire to design and fabricate ever smaller structures to improve device performance or achieve new device functionality, and of the limitations of more traditional experimental techniques in performing detailed and comprehensive characterization at the nanometer to atomic scale.

The unique and powerful advantage offered by STM and other scanning probe techniques is the ability to perform direct studies of structural, electronic, and other properties of materials with extremely high spatial resolution. Many other techniques, such as X-ray diffraction, electron diffraction, and transmission electron microscopy, typically provide only indirect information about sample structure and, while offering the ability to probe certain structural or compositional features at the atomic scale, inevitably average these properties over substantially larger areas or volumes. In scanning tunneling microscopy, however, direct imaging of features corresponding to individual atoms on a surface has been demonstrated for a wide range of materials. Other scanning probe techniques, while usually providing somewhat lower spatial resolution than STM, allow greater flexibility in samples that can be studied, imaging conditions that can be tolerated, and properties that can be characterized. Rapid progress in the development of new scanning probe techniques and in the commercial availability

S0009-2665(96)00084-2 CCC: $28.00

of scanning probe instrumentation has led to the widespread application of these techniques to problems of both scientific and technological importance.

Cross-sectional scanning tunneling microscopy has proven to be a particularly useful tool in the study of atomic-scale properties in III−V compound semiconductor heterostructures and of nanometer-scale structure and electronic properties in Si microelectronic devices. As characteristic dimensions in semiconductor devices continue to shrink and as advanced heterostructure devices increase in prominence, the ability to characterize structure and electronic properties at the atomic to nanometer scale has come to be of greater and greater importance. Cross-sectional STM offers unique capabilities for characterization that, in conjunction with a variety of other, complementary experimental methods, are providing new and important insights into material and device properties at the atomic to nanometer scale. In this review, we present a description of the basic experimental techniques involved in cross-sectional STM and a detailed discussion of the application of these techniques to the characterization of III−V and Group IV materials and device structures. Although not completely exhaustive, our review includes references to and descriptions of a wide range of cross-sectional STM work reported in the literature; in addition, detailed discussions of several results from our own laboratory are presented to illustrate the utility of cross-sectional STM for obtaining specific, detailed information about material and device structure at or near the atomic scale. We have focused specifically on cross-sectional STM as applied to the characterization of semiconductor epitaxial layers or device structures; studies in which the properties of generic cross-sectional semiconductor surfaces produced by cleaving are of primary interest are included only to the extent that issues of relevance to cross-sectional STM characterization of epitaxial layers and devices are addressed.

II. Sample Geometry and Surface Properties

In cross-sectional scanning tunneling microscopy, semiconductor wafers are cleaved to expose a cross section, typically a (110) or (111) plane, of epitaxial layers grown or device structures fabricated on the wafer. Scanning tunneling microscopy experiments performed on the cross-sectional surface can then reveal information about the atomic-scale morphology and electronic structure of these epitaxial layers or devices. The typical geometry of the sample and probe tip in cross-sectional STM are shown in Figure 1. Two factors are of critical importance in such experiments: first, the production of a cross-sectional surface that is atomically flat and as free as possible of surface states or defects that can act to pin the Fermi level at the surface; and second, the ability to position the tunneling tip reliably and reproducibly over specific regions of interest on the cross-sectional surface.

Production of an electronically unpinned surface, i.e., a surface at which the Fermi level is the same as that in the bulk rather than being determined exclusively by surface states, is a major consideration for spectroscopic studies of electronic structure in

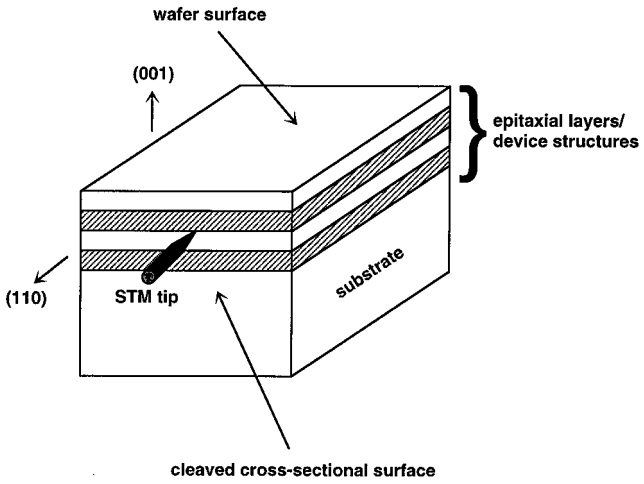

Figure 1. Sample and probe tip geometry in cross-sectional scanning tunneling microscopy. Typically, an (001) semiconductor wafer is cleaved to expose a (110) cross-sectional surface. Tunneling measurements are then performed with the STM tip positioned over the region of interest—generally consisting of exposed cross sections of epitaxial layers grown or devices fabricated on the top of the wafer—on the cross-sectional surface.

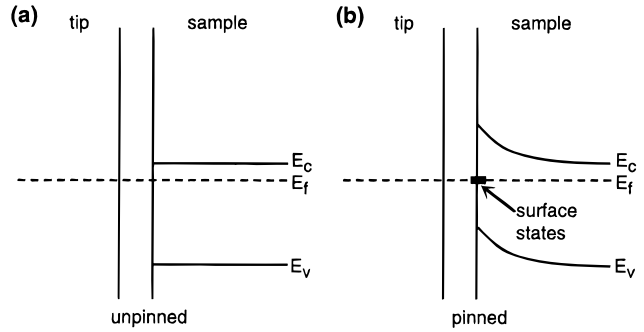

Figure 2. Schematic energy band diagram of an STM tip and semiconductor sample for (a) an unpinned and (b) a pinned semiconductor surface. For the unpinned surface, no surface states are present in the band gap and the Fermi energy at the surface assumes the same value as in the bulk material; for the pinned surface, surface states in the band gap force the Fermi energy to assume a specific value at the surface.

semiconductor heterostructures and devices. Figure 2 shows schematic energy band diagrams of an STM tip and sample for (a) an unpinned surface and (b) a pinned surface of a semiconductor sample. For the unpinned surface, no surface states are present in the band gap; the surface Fermi level is therefore the same as that in the bulk material. For the pinned surface, surface states in the band gap force the Fermi level to assume a specific value in the band gap, independent of its value in the bulk material. For most III−V semiconductors, an atomically flat (110) surface will not have surface states in the band gap and the surface will therefore be unpinned; defects such as monoatomic steps or contamination on the surface can produce dangling-bond states at energies in the band gap, leading to partial or complete pinning of the surface Fermi level. In scanning tunneling spectroscopy, described in detail in section III.b, the tunneling current is measured as a function of the bias voltage applied between sample and tip. For positive or negative bias voltage applied to the sample, tunneling of electrons occurs

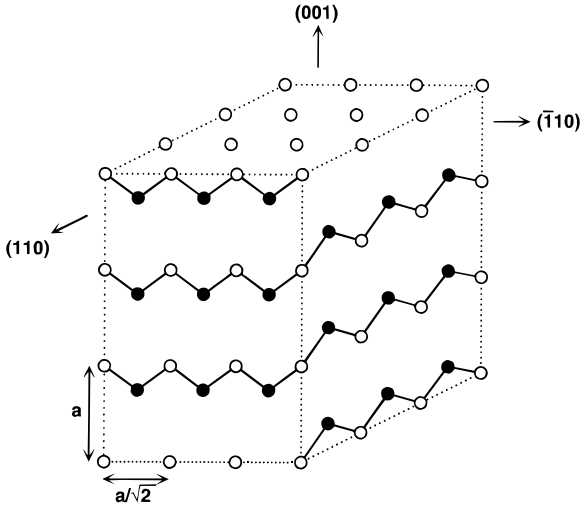

Figure 3. Schematic diagram of the zincblende crystal structure for the (001), (110), and (1̄10) lattice planes. *a* is the cubic lattice constant of the crystal (5.65 Å for GaAs). Empty and filled circles represent the cation and anion species, respectively, of a compound semiconductor. For III−V compound semiconductors, there is buckling of the lattice in the (110) and (1̄10) surface planes, but the surface unit cell remains 1×1. As-cleaved Si (110) surfaces are generally disordered and can undergo a variety of complex surface reconstructions.

between tip states and empty (conduction-band) or filled (valence-band) states, respectively, in the sample, allowing the detailed electronic structure of the sample to be probed.

A cross-sectional surface with the requisite structural quality can at present be obtained only by cleaving. III−V compound semiconductors cleave easily to yield a (110) surface that is atomically flat, with monolayer steps typically spaced tens to hundreds of nanometers apart. For Si and Si-based structures cleaving is more difficult, although flat (110) surfaces can be obtained. Figure 3 shows a schematic diagram of the (110), (1̄10), and (001) surfaces of a zincblende semiconductor crystal; *a* represents the cubic lattice constant of the semiconductor (e.g., 5.65 Å for GaAs). For a compound semiconductor, the empty and filled circles would correspond to the cation and anion species, respectively, e.g., the Group III (cation) and Group V (anion) species for a III−V compound semiconductor. For a Group IV elemental semiconductor all the atoms are, obviously, of the same valence. It should be noted that the definition of the (110) and (1̄10) cross-sectional planes used in some STM studies of (110) surfaces of III−V semiconductors[6] differs from that conventionally used in STM and other studies of epitaxial growth, in transport measurements, and other investigations. Some care must therefore be taken in comparison of STM characterization of (110) semiconductor surfaces with results of other studies.

As seen in Figure 3, the unreconstructed (110) and (1̄10) surface planes contain zigzag chains of atoms, with the cation and anion species alternating along each chain in a compound semiconductor. It may be seen from the figure that, for a compound semiconductor, the (110) and (1̄10) surface planes are inequivalent and, indeed, differences are observed between the two in, for example, the ease with which

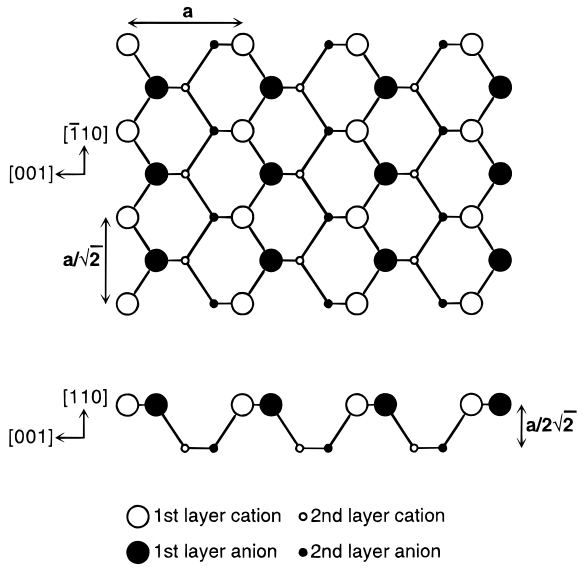

Figure 4. Structure of the top two atomic planes of the (110) surface for a zincblende crystal. In cross-sectional STM, atoms in the first layer are imaged directly, while those in the second layer are probed indirectly via their influence on the local electronic structure of the surface plane.

atomically flat cleaved surfaces can be produced. In a Group IV semiconductor the (110) and (1̄10) planes are of identical structure.

It is also worth noting that a given (110) surface plane contains atoms from only half of the (001) layers within the semiconductor crystal. As shown in Figure 4, the chains of atoms on the (110) surface are bonded to similar chains in a second layer located a distance $a/2\sqrt{2}$ below the surface plane. The atoms in the second layer are not imaged directly in cross-sectional STM, but do influence the contrast observed in cross-sectional STM imaging via their effect on the local electronic structure of the surface layer. Some possible effects of this aspect of the (110) surface structure are discussed in section IV.b.

For compound semiconductors, the cation and anion sites in the (110) and (1̄10) surface planes contain unoccupied and occupied dangling-bond states, respectively. STM imaging of the GaAs (110) surface has shown that for positive bias voltage applied to the sample, one obtains images of the unoccupied orbitals corresponding to the Ga (cation) sites on the (110) surface, while for negative sample bias voltage one images the occupied orbitals corresponding to the As (anion) sublattice on the (110) surface.[6] Figure 5 shows constant-current STM images from ref 6 of the GaAs (110) surface at positive and negative sample bias, clearly demonstrating bias-dependent, selective imaging of the Ga and As sublattices on the surface. Detailed STM studies of the GaAs (110) surface have shown that the surface unit cell remains 1×1, with the surface reconstruction consisting only of some buckling and bond reorientation.[6] Furthermore, scanning tunneling spectroscopy measurements have shown that for atomically flat (110) surfaces of GaAs and most other III−V compound semiconductors, surface states are not present in the band gap or at the band edges. These surfaces are therefore electronically unpinned, allowing the bulklike electronic properties of the sample at energies near the band

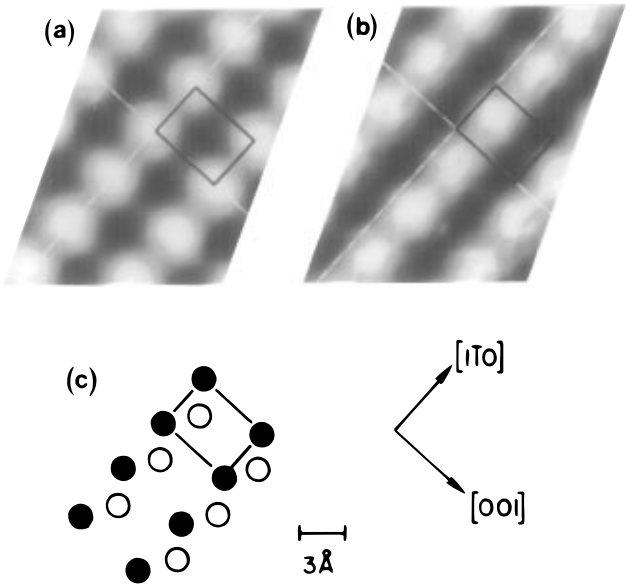

Figure 5. Constant-current STM images of the GaAs (110) surface obtained at (a) +1.9 V and (b) −1.9 V sample bias voltage. (c) Schematic diagram of atomic arrangement on the GaAs (110) surface; solid and empty circles represent Ga and As atoms, respectively. Comparison of the contrast observed in a and b within the rectangle representing the unit cell in the surface plane demonstrates that the Ga and As sites are selectively imaged for positive and negative sample bias, respectively. The cubic lattice constant for GaAs is $a = 5.65$ Å. (Reprinted from ref 6. Copyright 1987 American Institute of Physics.)

edges to be probed by tunneling spectroscopy.[7]

For Group IV elemental semiconductors, the as-cleaved (110) surface has been found to be disordered,[8] with complex surface reconstructions appearing upon annealing at high temperature.[9,10] However, hydrogen passivation of the (110) surface can be accomplished by dipping the cleaved wafer in hydrofluoric acid or by exposure of a clean, cleaved (110) surface to atomic hydrogen *in vacuo*, and is required to obtain a (110) surface that is not strongly pinned, i.e., a surface for which the density of surface states associated with defects or contamination is sufficiently low that the electronic properties of the bulk material can be probed using tunneling spectroscopy.

Positioning of the STM tip over the region of interest on the cross-sectional surface can be a nontrivial matter, as one is often interested in locating structures extending across ~1 μm or less on a cross-sectional surface that is a substantial fraction of a millimeter in width. One approach that has been used to locate epitaxial layers in such studies is to mount the STM in a scanning electron microscope (SEM).[11,12] By imaging the sample and tip using the SEM, it is possible to position the tip in the vicinity of epitaxially grown layers rapidly and reliably. An alternate method utilized by a number of researchers is shown in Figure 6. The tip is positioned as close as possible to the sample edge, and gradually moved toward the edge using the coarse positioning mechanism. When the tip has crossed over the sample edge, tunneling current can no longer be detected. The sample edge can then be used as a reference to locate the region of interest on the cross-sectional surface. This approach is most effective for samples consisting of epitaxial layers or

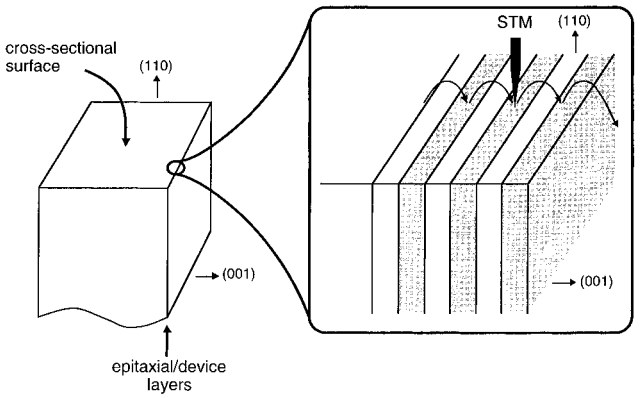

Figure 6. One procedure for locating epitaxial or device layers in cross-sectional scanning tunneling microscopy. The initial tunneling approach is made over the substrate region, which is easily visible in an optical microscope. The tip is then gradually stepped toward the edge, the location of which is signaled by a failure to detect tunneling current when the tip is advanced.

device structures on a conducting substrate (although its application is not precluded for samples on semi-insulating substrates[13]) and when a sharp, well-defined sample edge exists.

III. Imaging and Spectroscopy

Scanning tunneling microscopy provides information about the electronic structure of the sample under investigation via the dependence of the tunneling current on the tip−sample separation and on the local electronic densities of states in the sample and tip. A clear understanding of these dependences is essential for interpretation of cross-sectional STM data, and we therefore address this issue in some detail. For studies of semiconductor surfaces, the density of states in the tip may usually be assumed to be relatively featureless compared to that of the sample in the energy range of interest. This allows constant-current images, obtained by rastering the tunneling tip across the sample surface and, at each point, adjusting the tip−sample separation to yield a constant tunneling current, to be interpreted as profiles of the local electronic density of states of the sample. Details of the probe tip shape and cleanliness, however, can affect the appearance of such images, which must therefore be interpreted with appropriate caution.

Spectroscopic studies, in which the dependence of the tunneling current on tip−sample voltage, tip−sample separation, or other parameters is measured, can be used to probe the electronic properties of the tip−sample system with spatial resolution at or near the atomic scale. Detailed reviews of scanning tunneling spectroscopy can be found in refs 14−16. In this review we concentrate primarily on the aspects of spectroscopy of greatest relevance to studies of semiconductor electronic structure. It should be noted that spectroscopic measurements, to an even greater degree than constant-current imaging, are particularly sensitive to probe tip structure and cleanliness.[16] For example, relatively blunt tips, while not necessarily producing the highest spatial resolution in imaging, have been found to yield very consistent and reproducible spectroscopic results.[17]

a. Voltage-Dependent Imaging

The simplest extension of the constant-current imaging measurement described above is voltage-dependent imaging, in which constant-current images are obtained at different tip−sample bias voltages. Because of the dependence of the tunneling current on the tip and sample electronic densities of states, the tunneling current at different bias voltages will be dependent on the densities of states integrated over different ranges of energies. Contrast in the corresponding constant-current images will reflect these variations in electronic structure. In particular, positive bias applied to the sample will yield images of unoccupied electronic states on the sample surface, while negative sample bias will yield filled-state images. Some early examples of this approach include atom-selective imaging of the GaAs (110) surface[6] as described in section II, and studies of surface chemical bonding on clean and NH_3-dosed Si (001) surfaces.[18]

b. Scanning Tunneling Spectroscopy

Further information about the local electronic density of states on a sample surface can be obtained using techniques such as constant-separation spectroscopy, in which the feedback loop that maintains a constant tunneling current is momentarily disconnected and the tunneling current measured as a function of tip−sample bias voltage.[19−21] A detailed theoretical understanding of the dependence of the tunneling current on bias voltage and on the electronic structure of the sample and tip then allows current−voltage spectra obtained in this manner to be interpreted in terms of the local electronic density of states in the sample. In cross-sectional scanning tunneling microscopy performed on semiconductor heterostructures and devices, one often desires to obtain detailed, quantitative information about the structure and electronic properties of the sample under investigation. Because the electronic structure in such samples is often complex and highly inhomogeneous, especially at the nanometer scale, theoretical modeling and simulation of tunneling current−voltage spectra are likely to play an essential role in the detailed interpretation of both imaging and spectroscopic data.

The tunneling current $I(V)$ can be calculated using a variety of theoretical methods, two of which we describe here. In one approach, developed by Tersoff and Hamann,[22,23] the tunneling current is calculated from the transition rate between tip and sample states obtained using time-dependent perturbation theory. The total current arising from electrons tunneling both into and out of the sample is then given by

$$I(V) = \frac{2\pi e}{\hbar}\sum_{\mu,\nu}[f_t(E_\mu) - f_s(E_\nu + eV)] \times |M_{\mu\nu}|^2\,\delta(E_\mu - E_\nu) \quad (1)$$

where f_s and f_t are the Fermi distribution functions in the sample and tip, respectively, $M_{\mu\nu}$ is the quantum-mechanical tunneling matrix element between the tip state ψ_μ and the sample state ψ_ν, E_μ and E_ν are the energies of the states ψ_μ and ψ_ν, respectively, and $\delta(E_\mu - E_\nu)$ is the Dirac δ function. The sum is taken over all unperturbed tip and sample states. If the spectrum of states in the sample and that in the tip are continuous rather than discrete, the sum in eq 1 can be converted to an integral over energy

$$I(V) = \frac{4\pi e}{\hbar}\int \rho_t(E)\rho_s(E + \mathrm{eV}) \times [f_t(E) - f_s(E + eV)]|M_{\mu\nu}|^2\,\mathrm{d}E \quad (2)$$

where ρ_t and ρ_s are the electronic densities of states in the tip and sample, respectively. From eq 2 we see explicitly the dependence of the tunneling current on the densities of states in the tip and sample and on the tunneling matrix element. The tunneling matrix element $M_{\mu\nu}$ was shown by Bardeen[24] to be given by

$$M_{\mu\nu} = \frac{\hbar^2}{2m}\int \mathrm{d}\mathbf{S}\,(\psi_\mu^*\Delta\psi_\nu - \psi_\nu\Delta\psi_\mu^*) \quad (3)$$

where the integral is computed over a surface contained entirely within the vacuum barrier region.

Selloni et al.[25] and Lang[26] have suggested that, for nonzero bias voltages applied between the sample and tip, the tunneling current should be given approximately by an expression of the form

$$I(V) \propto \int_0^{eV}\rho_s(E)\rho_t(E - eV)T(E, V)\,\mathrm{d}E \quad (4)$$

where $T(E,V)$ is the transmission coefficient for electron transport between the sample and tip. The similarity between the expressions for $I(V)$ in eqs 2 and 4 is immediately evident, with $T(E,V)$ and $|M_{\mu\nu}|$ playing corresponding roles. If the electronic density of states in the tip is assumed to be constant, the conductivity derived from eq 4 is then given by

$$\frac{\mathrm{d}I}{\mathrm{d}V} \propto \rho_s(eV)\rho_t(0)T(eV,V) + \int_0^{eV}\rho_s(E)\rho_t(E - eV)\frac{\mathrm{d}T(E,V)}{\mathrm{d}V}\mathrm{d}E \quad (5)$$

The transmission coefficient in eqs 4 and 5 depends very strongly on the tip−sample separation and the tip−sample bias voltage; these dependences can obscure features in the current−voltage spectrum $I(V)$ and the conductivity $\mathrm{d}I/\mathrm{d}V$ arising from variations in the electronic density of states. Because the sample electronic density of states, $\rho_s(E)$, is most often the quantity of greatest interest, a procedure for extracting $\rho_s(E)$ from $I(V)$ and $\mathrm{d}I/\mathrm{d}V$ is highly desirable.

It has been shown[17,21] that a good approximation to the surface electronic density of states can be obtained from the normalized conductivity, $(\mathrm{d}I/\mathrm{d}V)/(I/V)$. From eqs 4 and 5 we can obtain an expression for the normalized conductivity

$$\frac{dI/dV}{I/V} \propto \frac{\rho_s(eV)\rho_t(0) + \int_0^{eV} \frac{\rho_s(E)\rho_t(E-eV)}{eT(eV,V)} \frac{dT(E,V)}{dV} dE}{\frac{1}{eV}\int_0^{eV} \rho_s(E)\rho_t(E-eV)\frac{T(E,V)}{T(eV,V)} dE} \quad (6)$$

Because the transmission coefficient appears in both the numerator and the denominator of both integrands, the dependence of the normalized conductivity on separation and voltage is much weaker than that of the current $I(V)$ or the conductivity dI/dV, and the normalized conductivity can be written in the form[14]

$$\frac{dI/dV}{I/V} = \frac{\rho_s(eV)\rho_t(0) + A(V)}{B(V)} \quad (7)$$

where $A(V)$ and $B(V)$ are slowly varying functions of V. Experimental studies have confirmed that the normalized conductivity has a much weaker dependence on tip−sample separation and applied voltage than does the conductivity dI/dV, and can provide a good approximation to the local electronic density of states.[17,21]

In another theoretical model, developed by Bono and Good,[27,28] the metal tip is modeled as a hemisphere of radius R projecting from a plane parallel to the sample surface. The probe tip is modeled as a free-electron metal, and the sample, in the case of a semiconductor, is assumed to be well described by an effective-mass model. The tunneling current for a voltage V applied to the tip is then given by[28]

$$I(V) = \frac{eA}{2\pi^2 h}\int dE[f_s(E) - f_t(E+eV)]\int d^2k_{||}T(E_\perp) \quad (8)$$

where $A = \pi R^2$ is the effective cross-sectional area of the tip, f_s and f_t are the Fermi distribution functions in the sample and tip, respectively, $k_{||}$ is the wave vector parallel to the sample surface, $E_\perp$ is the energy corresponding to the wave vector component normal to the sample surface, and $T(E_\perp)$ is the transmission coefficient. The integral is computed over all energies for which the electronic densities of states in the sample and tip are both nonzero. This approach has been used to develop semiquantitative simulations of current−voltage spectra for scanning tunneling spectroscopy performed on semiconductor surfaces.[7]

Theoretical models of the tunneling current such as those described above provide the basis for developing a detailed, quantitative understanding of the tunneling process. A comprehensive theoretical understanding of tunneling processes in STM and detailed simulations of tunneling currents for a variety of sample structures and experimental conditions will be essential for the most effective application of cross-sectional STM to the characterization of semiconductor materials and devices, particularly for heterostructure materials and advanced device structures in which the composition and electronic structure of the surface under investigation are spatially inhomogeneous and highly complex.

For studies of semiconductors, in which the presence of a nonzero band gap can lead to tunneling currents and conductivities ranging over several orders of magnitude, an additional issue of importance is dynamic range in the measurement of tunneling current. Wide dynamic range is especially important if features in the electronic density of states near or within the energy band gap are of interest. This issue has been addressed most effectively by the development and application of variable-separation spectroscopic techniques, in which the tunneling current is measured while both the tip−sample bias voltage V and the tip−sample separation s are varied in a controlled manner.[17,21,29] For example, a series of constant-separation current−voltage spectra can be measured at several different separations, or the separation may be varied continuously as the voltage is ramped. The variation in tip−sample separation is then accounted for by multiplication of the current by $e^{2\kappa\Delta s}$, where κ is the tunneling decay constant and Δs is the relative separation at which the tunneling current was measured. This factor represents the approximate change in tunneling probability associated with the change in separation Δs, and therefore allows tunneling currents measured at different tip−sample separations to be normalized, approximately, to a single, constant separation. Using this technique it is possible to measure values of the tunneling current over a limited dynamic range and, via the transformation described above, obtain the equivalent constant-separation current−voltage spectrum over a much larger range of current magnitude. A detailed discussion of variable-separation tunneling spectroscopy is presented in ref 16.

c. Spectroscopy on Unpinned Semiconductor Surfaces

Tunneling spectroscopy performed on unpinned surfaces of heavily doped semiconductors is of particular relevance to the characterization of semiconductor heterostructures and devices by cross-sectional STM. Unpinned surfaces, or at least surfaces that are not strongly pinned, are important for such applications because it is the electronic properties of the bulk material, rather than those arising predominantly from surface effects, that are of primary interest. For such surfaces, three components have been found to contribute to the tunneling current: tunneling of electrons from the tip into empty conduction-band states at large positive sample bias voltages, tunneling of electrons from filled valence-band states into empty tip states at large negative voltages, and tunneling involving dopant-induced carriers (electrons in the conduction band for *n*-type material or holes in the valence band for *p*-type) at voltages for which the Fermi level in the tip is at an energy aligned within the band gap of the sample.[7] Figure 7 shows current−voltage characteristics for tunneling on unpinned *p*-type and *n*-type Si surfaces calculated using the expression given in eq 4 for the tunneling current. The three components contributing to the tunneling current can be seen clearly in each case. Experimentally, it has been found that tunneling involving dopant-induced carriers can gen-

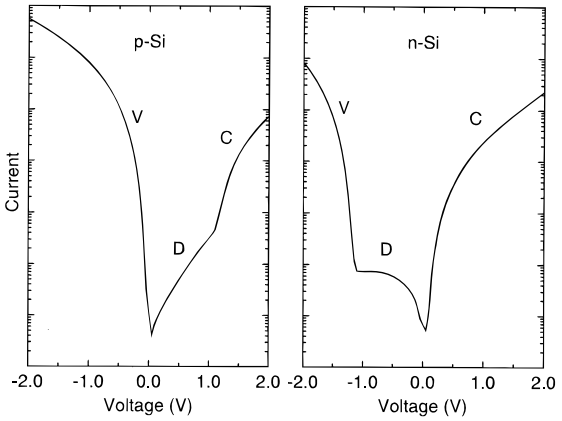

Figure 7. Current-voltage spectra for tunneling performed on unpinned surfaces of heavily-doped (1×10^{19} cm^{-3}) *p*-type and *n*-type Si, calculated using eq 4. Note the logarithmic scale used for the current axis. The conduction-band, valence-band, and dopant-induced components of the tunneling current, labeled C, V, and D, respectively, can be seen in each case.

erally be measured only for unpinned surfaces of very heavily doped material and that observation of the dopant-induced current is a good indication that a surface is electronically unpinned. However, the dopant-induced tunneling current is much smaller in magnitude than the conduction- and valence-band components, particularly for material with a substantial energy band gap; resolving this component in spectroscopic measurements therefore requires that the tunneling current be measured over a large dynamic range.

Feenstra[30] has performed detailed scanning tunneling spectroscopy measurements on cleaved (110) surfaces of several III−V semiconductors. III−V semiconductors are particularly well suited for such studies, as they cleave easily to yield atomically flat and, for most III−V semiconductors, electronically unpinned (110) surfaces ideally suited for tunneling measurements. Detailed tunneling current spectra were obtained for GaAs, InP, GaSb, InAs, and InSb using variable-separation spectroscopy. Figure 8 shows normalized conductivities measured for cleaved (110) surfaces of several III−V semiconductors. In these spectra, the conduction-band and valence-band edges, *L*-point band edges, and features associated with surface states can be distinguished; the energies of these features can be determined to within ±0.03 eV, with shifts in energies arising from tip-induced band bending estimated to be less than 0.1 eV for dopant concentrations higher than $\sim 1 \times 10^{18}$ cm^{-3}. For samples in which the dopant concentration is substantially lower, tip-induced band bending can shift the apparent energies of the band edges by as much as several tenths of an electron volt, making accurate, quantitative interpretation of features observed in current−voltage spectra considerably more difficult.

d. Current Imaging Tunneling Spectroscopy

Spatially resolved spectroscopic measurements can be used to construct images that reveal atomic- to nanometer-scale variations in electronic structure on the sample surface. In one such technique, referred

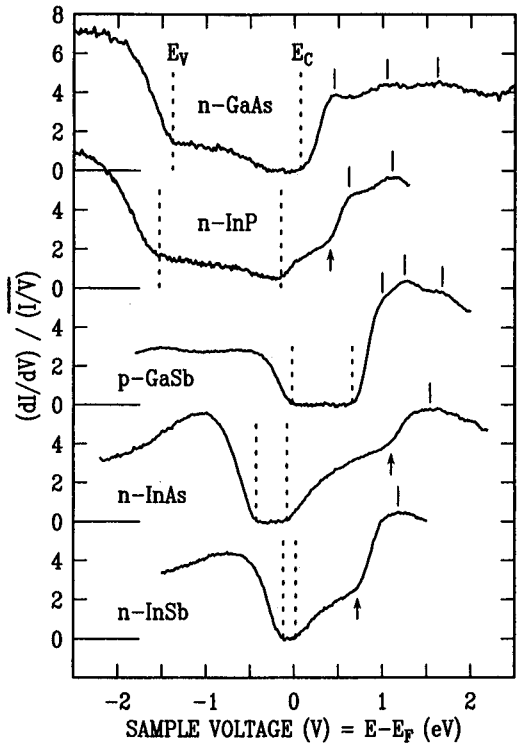

Figure 8. Normalized conductivities measured by scanning tunneling spectroscopy for cleaved (110) surfaces of *n*-GaAs, *n*-InP, *p*-GaSb, *n*-InAs, and *n*-InSb. Valence-band-edge and conduction-band-edge energies E_V and E_C, respectively, are indicated by dashed lines; L-valley conduction-band energies are indicated by the arrows, and various surface states by solid lines. The energies of these features can be determined to within approximately ±0.03 eV. (Reprinted from ref 30. Copyright 1995 American Institute of Physics.)

to as current imaging tunneling spectroscopy (CITS), a constant-current topographic scan with the current stabilized at a fixed value I_0 for a specific voltage V_0 is performed over the sample surface and, at each point, a current−voltage spectrum is measured. Variations in electronic structure across the sample surface will produce corresponding variations in the current−voltage spectra; these spatial variations can then be revealed by plotting the current measured at specific bias voltages other than V_0—so-called "current images". Hamers et al.[20] first used this technique to study atomic-scale variations in the electronic structure of the 7×7 reconstruction of the Si (111) surface.

Current images cannot, however, necessarily be interpreted as direct images of particular features in the local electronic density of states. Because the tip−sample separation at each point is determined by the constant-current condition at a single bias voltage V_0, topographic and electronic information may be difficult to distinguish from each other in a CITS measurement. Contrast in current images can in fact be caused both by localized variations in electronic structure and by changes in the background of the spectrum that can arise from, for example, the dependence of the tunneling probability on separation. Hamers et al.[20] have argued that, for CITS performed with a constant-current bias voltage V_0 that produces a topographic image reflecting primarily the actual physical topography of the

sample surface, constrast in current images will reflect primarily differences in electronic structure. Satisfying this condition, however, requires a detailed prior knowledge of the physical topography of the surface. Indeed, studies of the Si (111) 2×1 surface by Stroscio et al.[31,32] showed explicitly that contrast in current images can arise from topographically induced changes in the tunneling probability as well as variations in the electronic density of states; however, it was also noted that these effects could be reduced by generating images of the normalized conductivity $(dI/dV)/(I/V)$ rather than simply the tunneling current I.

From this discussion it should be apparent that imaging and tunneling spectroscopy are extremely powerful tools for probing the structure and electronic properties of conducting or semiconducting samples, but also that considerable care is required in performing and interpreting such measurements. Continued advances, particularly in the application of tunneling spectroscopy to advanced semiconductor materials and device structures, are likely to require further improvements in sample and probe tip preparation, continued development and implementation of advanced techniques such as variable-separation spectroscopy, and perhaps most important, the development of a more complete understanding of the relationship between the measured tunneling current and the detailed electronic structure of the sample and tip. This is particularly true for complex, highly inhomogeneous sample structures that are likely to be encountered in technological applications.

IV. III–V Semiconductor Characterization

The development of epitaxial crystal growth techniques such as molecular-beam epitaxy (MBE) combined with great flexibility in choice of materials has allowed semiconductor heterostructure device concepts to be explored extensively in III−V compound semiconductor material systems. Advances in heterostructure materials and device technology have depended to a considerable degree upon studies of, and consequently improvements in, crystal growth techniques and the resulting structure of epitaxially grown layers. As material quality has improved and as device structures have grown in sophistication, it has become increasingly apparent that an understanding of, and ultimately control over, growth processes and epitaxial layer structure at the atomic scale will be needed for realization and optimization of advanced semiconductor heterostructure and nanoscale devices.

III−V semiconductors are in many ways ideally suited for study by cross-sectional STM. Cleaving of (001) wafers can produce (110) cross-sectional surfaces with atomically flat planes extending over tens to hundreds of nanometers. To avoid contamination of the cleaved surface, cleaving under ultra-high vacuum conditions is necessary. Furthermore, for atomically flat (110) surfaces of most III−V materials[33,34]—GaP being a notable exception[35−37]—the Fermi level at the surface is unpinned, and tunneling spectroscopy performed on the surface can yield information about the electronic properties of the bulk material.

The first cross-sectional STM experiments in which actual epitaxial and device structures were investigated were performed by Muralt et al.[38−40] In these studies, scanning tunneling microscopy and potentiometry were used to probe potential distributions in a GaAs *pn* junction and a GaAs/$Al_{0.40}Ga_{0.60}As$ double-heterojunction laser structure. Salemink et al. performed the first studies in which a GaAs/$Al_xGa_{1-x}As$ heterojunction interface was resolved directly by scanning tunneling spectroscopy,[41] and subsequently extended this work to obtain the first atomically resolved images of GaAs/$Al_xGa_{1-x}As$ heterostructures.[42−45] To date, a number of groups have reported scanning tunneling microscopy studies, both in air and under ultrahigh-vacuum conditions, of epitaxially grown structures in a wide range of material systems.

a. Electronically Induced Topographic Contrast

In constant-current cross-sectional images of heterostructures, apparent "topographic" contrast between the different materials present in the heterostructure is typically observed, with corrugation amplitudes ranging from less than 1 Å to over 100 Å. This contrast is generally ascribed to differences in the electronic properties of the constituent materials, rather than to actual physical topography. Factors such as differing energy band gaps, dopant and carrier concentrations, and electron affinities can contribute to the apparent topographic contrast between materials in a heterostructure, with variations in band-edge energy from one layer to the next generally being the dominant contributing factor to the observed heterostructure contrast.

To explain the electronically induced topographic contrast observed in such images, we note that the tunneling current integral in eq 2 includes factors for the densities of states in the tip and sample and for the difference between the Fermi distribution function in the sample and that in the tip. At bias voltages typically applied for tunneling in semiconductors, the main contribution to the tunneling current will therefore involve an integral of the sample density of states over the energy range between the Fermi energies in the sample and tip. This contribution to the tunneling current will vary from layer to layer in a heterostructure because of the changes in electronic structure from one material to the next. In constant-current imaging, these variations are manifested as changes in the apparent topographic height of the surface as the tip−sample separation is adjusted to yield a constant tunneling current at each point. In complex structures such as superlattices, in which the electronic structure changes considerably from that in bulk material, these effects can become more complex; however, the basic principle remains valid.

Figure 9 shows the band-edge energy structure and a cross-sectional STM image, obtained at negative sample bias, of an InAs/$InAs_{1-x}Sb_x$ superlattice. As shown in the band-edge energy diagram, tunneling of valence-band electrons from the sample into empty tip states occurs over a wider range of energy in the $InAs_{1-x}Sb_x$ layers than in the InAs layers for negative bias voltage applied to the sample. Consequently,

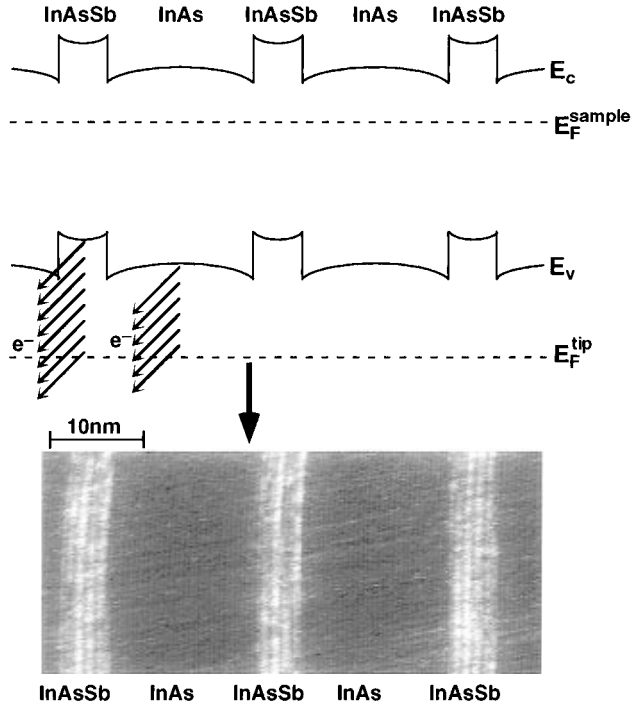

Figure 9. Current flow, and the resulting topographic image for negative sample bias voltage, in cross-sectional scanning tunneling microscopy performed on an InAs/$InAs_{1-x}Sb_x$ heterostructure. For negative bias voltage applied to the sample, the tip Fermi level, E_F^{tip}, will be below the sample Fermi level, E_F^{sample}, and tunneling of electrons will occur from filled (valence-band) states in the sample into empty states in the tip. The arrows provide a schematic indication of the tunneling current arising from carriers in the sample at energies between the Fermi levels in the sample and tip. Because the electronic structure changes from one layer of the heterostructure to the next, the tunneling current measured for a fixed tip−sample separation would vary accordingly. In constant-current imaging, the tip−sample separation is adjusted to yield a constant tunneling current, resulting in electronically induced topographic contrast as seen in the image.

maintaining a constant tunneling current requires that the tip−sample separation be increased when the tip is located over the $InAs_{1-x}Sb_x$ layers, leading to an apparent difference in topographic height. Furthermore, an additional periodic structure is visible within each $InAs_{1-x}Sb_x$ layer. This contrast arises from the periodic compositional structure within each $InAs_{1-x}Sb_x$ layer induced by the modulated MBE technique[46,47] employed during the growth of the $InAs_{1-x}Sb_x$ layers in the superlattice. In this growth technique, the average group V composition in the $InAs_{1-x}Sb_x$ alloy layer is controlled by growing alternating layers of InAs and InSb rather than a random alloy, resulting in the periodic structure evident in the cross-sectional STM image. Detailed studies of this structure are described in section IV.d.

The wide range of height differences from layer to layer reported by different investigators for cross-sectional STM imaging of semiconductor heterostructures is likely to be due at least in part to variations in tip and sample cleanliness. If excessive contamination is present on the tip or sample, the apparent barrier height will be anomalously low and the change in tip−sample separation required to maintain a constant tunneling current will be much larger than that for an ideal vacuum barrier. Furthermore, different rates of oxidation in air for different materials in a heterostructure can lead to actual physical topography that is correlated with composition. The latter phenomenon has been observed in AFM studies of $GaAs/Al_xGa_{1-x}As$ heterostructures.[48] In addition, STM studies of InGaAs/InP multiple quantum wells conducted in air revealed that observations of large (several nanometers or more) heterostructure corrugation amplitudes were correlated with low apparent barrier heights and with increases in ambient humidity.[49]

Cross-sectional STM offers unique capabilities for characterization of atomic-scale structure in semiconductor alloy layers and at heterojunction interfaces. It has been noted[45,50] that because STM imaging is sensitive primarily to the one or two uppermost layers on the surface, atomic-scale features in structure and electronic properties can be resolved with considerably greater detail than in other techniques. High-resolution X-ray diffraction can in some circumstances yield information about atomic-scale interface structure in superlattices,[51,52] but this information is inevitably averaged over many layers and also over a large area of the sample. Transmission electron microscopy (TEM), particularly the chemical lattice imaging technique,[53−55] can provide information about atomic-scale interface structure, but averaging that occurs through the thickness of the sample—typically on the order of 100 Å or more—limits the technique's ability to resolve features such as atomic-scale interface roughness and fluctuations in composition.

Atomically resolved imaging of cross-sectional surfaces, which thus far has been achieved only for III−V semiconductors and under ultra-high vacuum conditions, is therefore a uniquely powerful tool for exploring alloy layer and heterojunction interface structure at the atomic scale. Constant-current images of cross-sectional surfaces are sensitive primarily to composition within the atomic plane at the surface, and to a limited degree to composition a few to several layers below the surface. Compositional fluctuations at the atomic scale, which would be undetectable using other characterization techniques due to averaging effects, are therefore clearly visible in high-resolution cross-sectional images. By combining information obtained from cross-sectional STM with results obtained using complementary characterization techniques such as X-ray diffraction, electron diffraction, electron microscopy, and electrical and optical measurements, one is able to develop a detailed understanding of atomic- to nanometer-scale properties of semiconductor materials and devices, confirm that this information is representative of properties at the larger length scales relevant for most device structures, and ultimately establish correlations between atomic-scale material properties and the behavior of actual devices.

b. GaAs/AlGaAs Heterostructures

Characterization of $GaAs/Al_xGa_{1-x}As$ heterojunctions using cross-sectional STM performed under ultrahigh vacuum conditions has proven to be a powerful probe of atomic-scale alloy layer and inter-

face structure. Studies of GaAs/Al_xGa_{1-x}As heterostructures either cleaved and imaged in air[56] or cleaved in air and imaged in vacuum[57] have yielded constant-current images in which apparent contrast between the GaAs and Al_xGa_{1-x}As layers was observed, but with substantially lower resolution than that achievable for cleaving and imaging performed entirely under ultrahigh vacuum conditions.

The first atomically resolved images of semiconductor heterostructures in cross-sectional scanning tunneling microscopy were obtained by Salemink et al. in studies of GaAs/Al_xGa_{1-x}As heterostructures under ultrahigh-vacuum conditions.[42−45] In these and subsequent studies, Albrektsen et al.[45,58] were able to determine the locations of heterojunction interfaces with a precision of ±1 unit cell, allowing monolayer steps at the interfaces to be resolved. These studies yielded direct images of step bunching and consequent terrace formation at GaAs/Al_xGa_{1-x}As interfaces for heterostructures grown on GaAs (001) substrates with a 2° miscut in the [1$\bar{1}$0] direction.[45] Cross-sectional STM has also revealed the presence of atomic-scale fluctuations in the composition of ternary III−V alloys. In studies of GaAs/Al_xGa_{1-x}As heterojunctions, Albrektsen et al.[58] observed nanometer-scale "mottling" in constant-current images of the Al_xGa_{1-x}As layers, indicative of nonuniformity in the electronic structure of the alloy that was tentatively attributed to fluctuations in composition. Detailed imaging of a GaAs/$Al_{0.35}Ga_{0.65}$As/GaAs structure by Salemink and Albrektsen[59] revealed clustering of Al atoms in the ternary alloy with a typical length scale estimated to be two to three unit cells (10−15 Å). Further studies by Johnson et al.[60] confirmed these observations of interface roughness and alloy fluctuations, and revealed Al-rich regions running along the [$\bar{1}$12] and [1$\bar{1}$2] directions (as observed on the (110) cross-sectional surface); the latter observation was interpreted as possible evidence for preferential growth of Al-rich regions aligned along these directions in the Al_xGa_{1-x}As layers. Figure 10 shows an atomically resolved filled-state cross-sectional image of a GaAs/Al_xGa_{1-x}As/GaAs heterostructure, obtained at −2.1 V sample bias and 0.1 nA tunneling current. The Al_xGa_{1-x}As layer is clearly lower topographically, on average, than the surrounding GaAs layers, consistent with the valence-band-edge discontinuity at the heterojunction interface. In addition, local atomic-scale contrast within the Al_xGa_{1-x}As layer can arise from the bonding of the surface As atoms to both Al and Ga atoms on the surface and one layer below, although the atomic-scale features visible in the image correspond to occupied orbitals on the Group V (As) sublattice of the (110) cross-sectional surface. Mottling in the Al_xGa_{1-x}As layer may therefore be interpreted as reflecting local variations in the Al concentration within the ternary alloy layer.

A dependence of interface structure in GaAs/Al_xGa_{1-x}As heterojunctions on growth sequence and growth conditions in molecular-beam epitaxy has also been observed by cross-sectional STM. Smith et al.[61,62] have performed ultrahigh-vacuum cross-sectional STM studies of GaAs/$Al_{0.3}Ga_{0.7}$As superlattices and observed that interface roughness amplitudes were greater by approximately 10 Å for the inverted (GaAs-on-$Al_{0.3}Ga_{0.7}$As) interface compared to the normal ($Al_{0.3}Ga_{0.7}$As-on-GaAs) interface. Studies of AlAs/GaAs short-period superlattices revealed that incorporation of 30 s growth interrupts at each interface substantially improved interface abruptness compared to that achieved with 5 s growth interrupts.[62,63] Also addressed in these studies was the influence of bonding configuration on the (110) surface on atomic-scale contrast observed by cross-sectional STM.[63] Figure 11 shows the four possible arrangements of Al, Ga, and As atomic layers for a (110) cross section of a GaAs/AlAs interface. The numbers to the left of each first-level As layer indicate the number of Al atoms to which the As atoms in that layer are bonded. Since only the first-level As atoms are imaged directly for cross-sectional STM imaging performed at negative sample bias—as is often the case for III−V semiconductors—four possible sequences of bonding configurations for successive first-layer As rows may be present at a given interface. Thus, even for interfaces that, as shown in Figure 11, are all perfectly abrupt, the apparent interface abruptness observed in a filled-state cross-sectional STM image may vary slightly with the atomic configuration at the (110) surface.

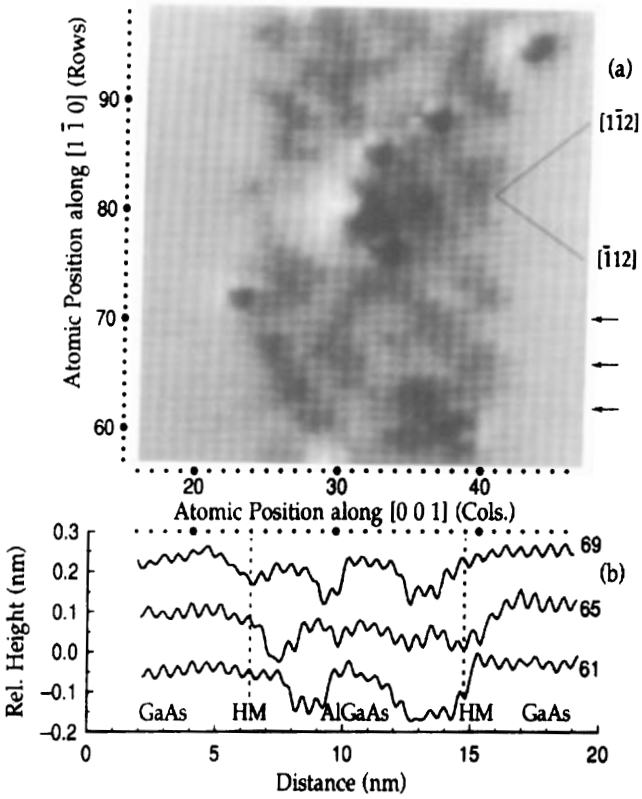

Figure 10. Atomically resolved filled-state cross-sectional STM image of a GaAs/Al_xGa_{1-x}As/GaAs heterostructure, obtained at −2.1 V sample bias and 0.1 nA tunneling current. Topographic line scans along the rows indicated are shown below the image. The average topographic height within the Al_xGa_{1-x}As layer is clearly lower than in the surrounding GaAs, reflecting the change in electronic structure across the interface. Mottling in the Al_xGa_{1-x}As layer reflects local variations in Al concentration. (Reprinted from ref 60. Copyright 1993 American Institute of Physics.)

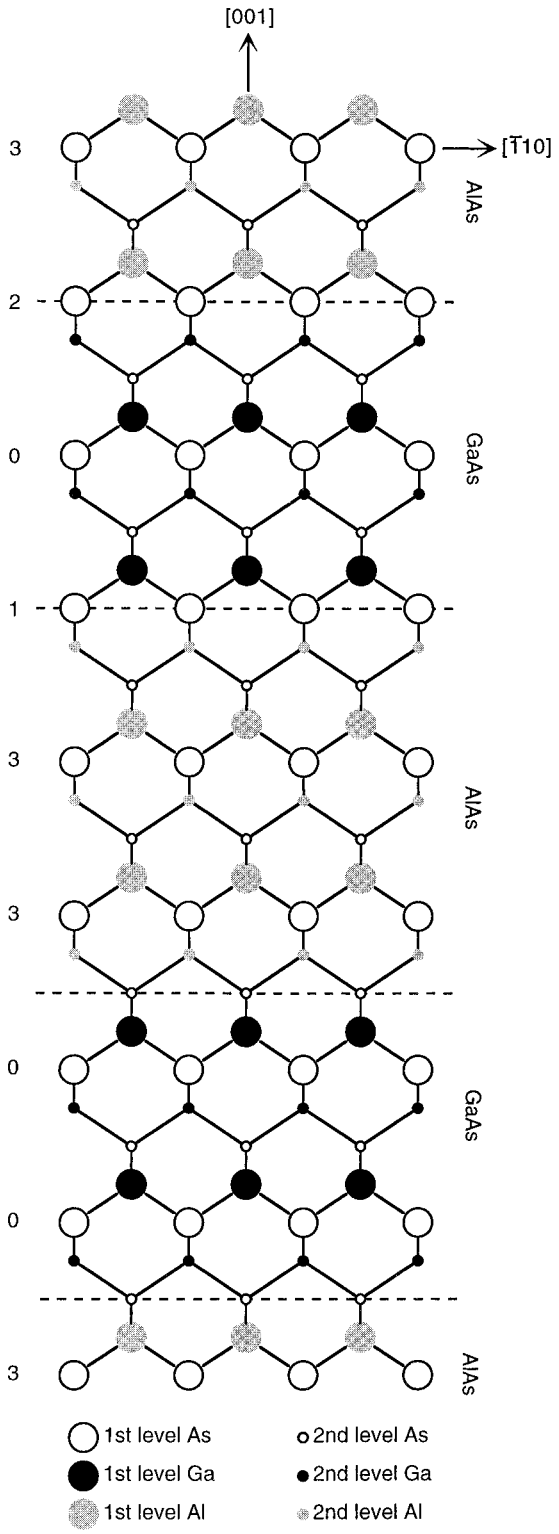

Figure 11. Arrangement of atoms at the (110) surface for an AlAs/GaAs heterostructure. The precise location of each AlAs/GaAs interface, indicated by the dashed lines, with respect to the first-level As atoms influences the bonding configurations for the first-level As rows near the interface, and may consequently affect the apparent interface abruptness observed in a cross-sectional STM image. Such differences would be artifacts of the cross-sectional STM technique, since all the interfaces shown are atomically sharp.

c. GaAs/InGaAs Heterostructures

The detailed structure of GaAs/$In_xGa_{1-x}As$ interfaces is of considerable importance for heterostructure devices such as pseudomorphic modulation-doped field effect transistors (MODFET's) and quantum-well and quantum-wire lasers. For electronic devices, such as MODFET's, based on lateral transport of carriers near a heterojunction interface, local composition variations and interface roughness can significantly affect carrier mobility and, consequently, device performance. For quantum-well- and quantum-wire-based optoelectronic devices, precise control over layer thickness and alloy composition is essential to ensure optimum device performance at specific wavelengths. Clustering of In and asymmetric interface broadening have been observed by STM in cross-sectional studies of GaAs/$In_xGa_{1-x}As$ heterostructures performed by Zheng et al.[64] Figure 12 shows an empty-state cross-sectional STM image of a pseudomorphic GaAs/$In_xGa_{1-x}As$ multiple-quantum-well structure grown by MBE. Chainlike clusters containing 2−3 In atoms aligned in the [001] direction are observed in coherently strained $In_{0.20}Ga_{0.80}As$ layers grown on GaAs (001) substrates. In addition, segregation of In on the growth surface was found to produce asymmetric broadening at the GaAs/$In_{0.20}Ga_{0.80}As$ interfaces. For $In_{0.20}Ga_{0.80}As$ grown on GaAs, the interfaces were found to be 2−4 atomic

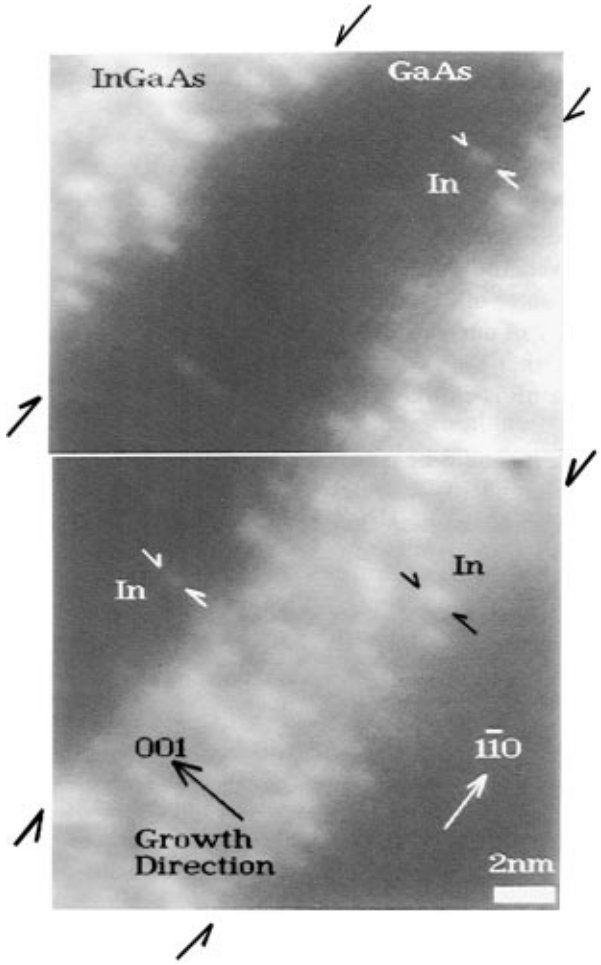

Figure 12. Cross-sectional STM image, obtained at a sample bias of +2.0 V and a tunneling current of 0.5 nA, of a GaAs/$In_{0.2}Ga_{0.8}As$ multiple-quantum-well structure. Asymmetric broadening of the GaAs/$In_{0.2}Ga_{0.8}As$ interfaces arising from In segregation during growth is observed, as is the formation of 2−3 atom In clusters (indicated by arrows) aligned along the [001] direction. (Reprinted from ref 64. Copyright 1994 American Institute of Physics.)

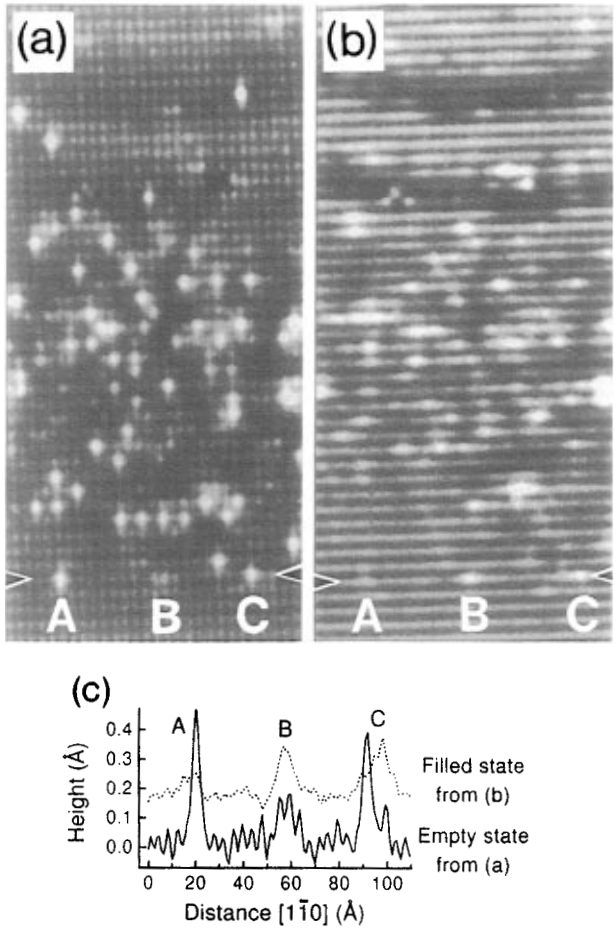

Figure 13. (a) Empty-state and (b) filled-state images of a 112 Å × 250 Å region of an $In_xGa_{1-x}As$ quantum-wire structure surrounded by $(AlAs)_4(GaAs)_4$ superlattice barriers. The images are of the exact same cross-sectional area of the quantum-wire structure. (c) Topographic profiles from the empty-state and filled-state images along the lines indicated by the arrows. (Reprinted from ref 65. Copyright 1995 American Institute of Physics.)

layers wide; for the opposite growth sequence, incorporation of excess In segregated on the growth surface was believed to be responsible for producing interfaces extending over 5−10 atomic layers. This asymmetry in the structure of the GaAs/$In_{0.20}Ga_{0.80}$As interfaces is qualitatively apparent in the image shown in Figure 12, and has been confirmed by quantitative determination of In concentration as a function of position in the [001] growth direction.[64]

In cross-sectional STM studies performed by Pfister et al.[65] of $In_xGa_{1-x}As$ quantum wells and $In_xGa_{1-x}As$ quantum wires embedded in $(AlAs)_4(GaAs)_4$ superlattice barriers grown on V-groove-patterned GaAs (001) substrates, substantial segregation of In from the $In_xGa_{1-x}As$ quantum well and incorporation of In into the subsequently grown $(AlAs)_4(GaAs)_4$ barrier was also observed. However, no In clustering beyond that expected statistically for a random alloy was detected, nor was evidence seen for preferential In incorporation at the center of the quantum wire. Studies of $In_xGa_{1-x}As$ quantum-wire structures by Pfister et al.[65] have also demonstrated the possibility of performing quantitative chemical identification of atoms in the surface and first subsurface layers of the (110) cleaved cross-sectional plane for ternary III−V alloys. Figure 13 shows empty-state and filled-state images of an $In_xGa_{1-x}As$ quantum-wire structure surrounded by $(AlAs)_4(GaAs)_4$ superlattice barriers. In the empty-state image, bright spots are observed that correspond to unoccupied In orbitals on the (110) surface; fainter features in the empty-state image appear to correspond to In atoms in the first subsurface layer. In the filled-state image, bright spots appear to correspond primarily to filled As orbitals associated with As atoms back-bonded to In atoms in the first subsurface layer which cause the surface As atoms to protrude from the surface plane, yielding the observed contrast. These interpretations are supported by comparisons of filled-state and empty-state images of identical areas: the bright As sites are correlated with faint double-site features in the empty-state image, and surface In atoms visible in the empty-state image produce only weak contrast in the filled-state image for As atoms to which they are bonded.

d. Arsenide/Antimonide Heterojunctions

Mixed-anion material systems, in which the Group V as well as the Group III constituent changes across a heterojunction interface, are particularly rich in possibilities for complex interfacial structure. In these material systems, two distinct bond configurations—both of which correspond to a structurally perfect heterojunction—can be present at each interface.[66] The InAs/AlSb heterojunction, for example, can contain either InSb-like or AlAs-like bonds at the interface. Furthermore, it has been demonstrated that interfacial composition can exert a considerable influence on electron transport[66] and optical properties[67] in InAs/AlSb quantum wells and superlattices, and on the superlattice band gap and background doping characteristics of InAs/$Ga_{1-x}In_xSb$ superlattices.[68]

Cross-sectional STM studies of InAs/GaSb[69−71] and InAs/$Ga_{1-x}In_xSb$[72,73] superlattices have begun to provide insight into some of these issues. A cross-sectional constant-current STM image of an InAs/$Ga_{0.75}In_{0.25}Sb$ superlattice is shown in Figure 14. Atomic-scale interface roughness is clearly visible in the image, as is a dependence of the InAs/$Ga_{1-x}In_x$Sb interface structure on growth sequence. Detailed studies of InAs/GaSb and InAs/$Ga_{1-x}In_xSb$ superlattices have revealed clear evidence, in both spectroscopy[69,70] and imaging,[72,73] of a dependence of interfacial electronic structure on interface growth sequence; such an asymmetry could arise from a number of sources. In studies of InAs/GaSb superlattices, Feenstra et al.[69−71] attributed the observed asymmetry to incorporation of Sb riding on the growth surface into InAs grown on GaSb. Lew et al.[72,73] have suggested that an additional factor may be the asymmetry in superlattice electronic structure that can arise if different interfacial bond configurations are formed for different growth sequences.

Quantitative information about atomic-scale interface roughness can be obtained very effectively by cross-sectional STM. Feenstra et al.[69−71] have performed quantitative studies of interface roughness in InAs/GaSb superlattices as a function of MBE growth conditions. Fourier spectra computed for heterojunction interface profiles obtained from InAs/

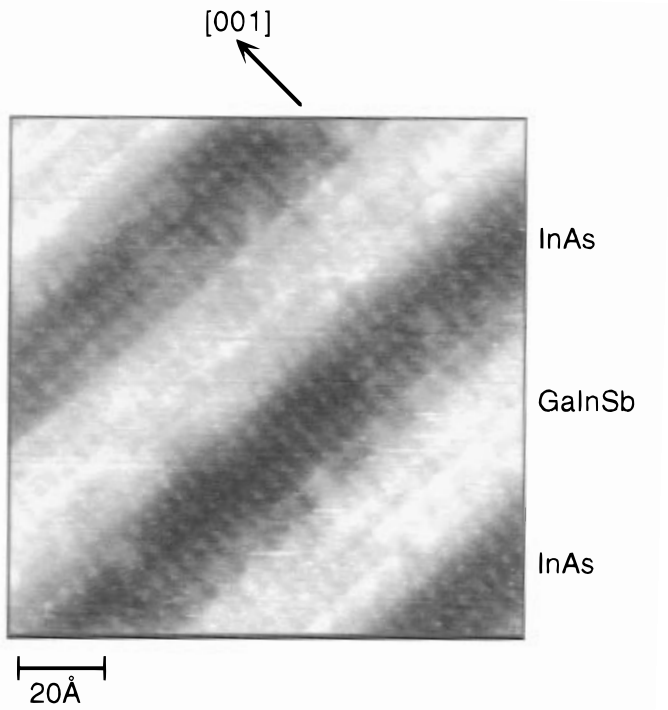

Figure 14. Cross-sectional STM image of an InAs/$Ga_{0.75}In_{0.25}Sb$ strained-layer superlattice, obtained at a sample bias of −1.5 V and a tunneling current of 0.1 nA. The bright and dark regions correspond to the $Ga_{0.75}In_{0.25}Sb$ and InAs layers, respectively. Features corresponding to individual atomic orbitals on the Group V sublattice of the cleaved (110) surface are clearly visible, allowing phenomena such as atomic-scale interface roughness and atomic cross-incorporation to be investigated.

GaSb superlattices were found to be consistent with a Lorentzian spectral distribution expected to be characteristic of interfaces with random step distributions. A significant dependence of interface structure on growth sequence was observed, with InAs-on-GaSb interfaces being significantly rougher than those in which GaSb was grown on InAs. This dependence of interface roughness on growth sequence was attributed to incorporation of excess Sb from the GaSb growth surface into the subsequently grown InAs layer. Consistent with this interpretation, growth by atomic-layer epitaxy and growth at higher substrate temperatures (460 °C vs 380 °C) were found to yield significant reductions in interface roughness.

As an illustration of the quantitative analysis of interface roughness using cross-sectional STM, we describe studies by Lew et al.[74] of the dependence of interface roughness in InAs/$Ga_{1-x}In_xSb$ superlattices on orientation and growth sequence. Figure 15a shows a cross-sectional STM image of a 17 Å InAs/50Å $Ga_{0.75}In_{0.25}Sb$ superlattice grown on a GaSb (001) substrate. Interfaces between the InAs (dark) and $Ga_{0.75}In_{0.25}Sb$ (bright) layers can be extracted from images of both (110) and $(1\bar{1}0)$ surfaces by enhancing the grey-scale contrast in the image and employing an edge-detection algorithm to identify the interfaces. Figure 15, parts b and c, show representative interfaces extracted in this manner from images of the (110) and $(1\bar{1}0)$ surfaces, respectively. Analysis of images in this manner allows detailed, quantitative information about interface structure, and its dependence on orientation and growth sequence, to be

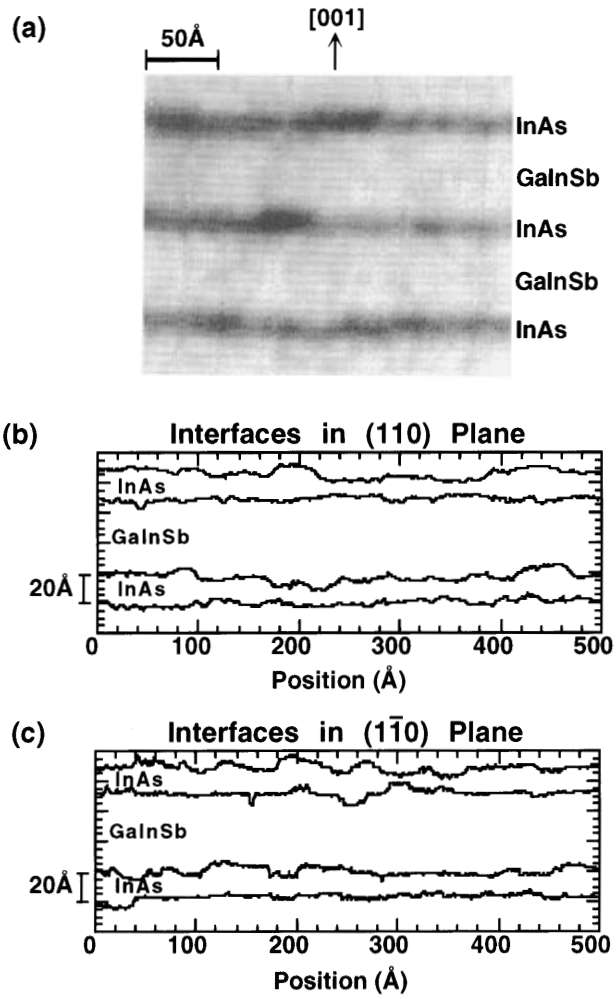

Figure 15. (a) Cross-sectional STM image of a 17 Å InAs/50 Å $Ga_{0.75}In_{0.25}Sb$ superlattice, obtained at a sample bias of −1.5 V and a tunneling current of 0.1 nA. (b) Profiles of heterojunction interfaces in the superlattice extracted from a (110) cross-sectional STM image of the superlattice; (c) heterojunction interface profiles extracted from a (110) cross-sectional STM image.

obtained. Considerable care must be taken, however, to ensure that interface profiles extracted from cross-sectional STM images are independent of the method of interface definition and extraction. While the method employed by Lew et al.[74] was checked to ensure that this criterion was satisfied, it is necessary to note that, at the atomic scale, inherent ambiguity in the definition of heterojunction interfaces can arise from the fundamental structure of the interface region, e.g., if atomic-scale intermixing or grading is present; this should be distinguished from the experimental uncertainty that can arise from the technique used to extract the interface profile from the STM image.

Interface roughness in these structures can be quantified by performing a Fourier analysis of the interface profiles extracted from the cross-sectional STM images. Given a real-space interface profile $a(x)$, one may calculate a discrete Fourier transform to obtain the spectral components, A_q, of the roughness amplitude. The roughness amplitude components A_q are then given by

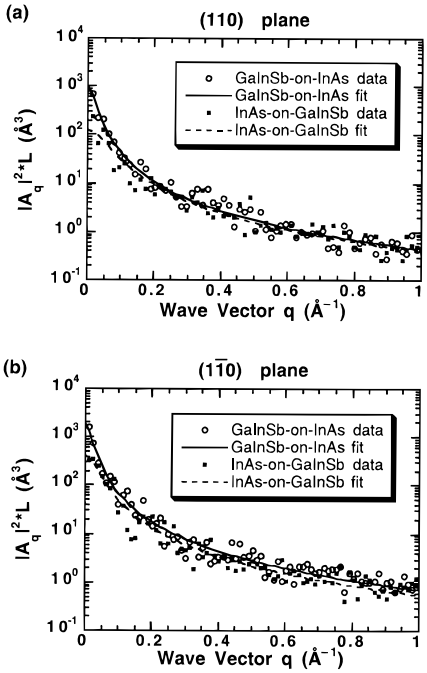

(c)

Plane	Interface	Δ (Å)	Λ (Å)
(110)	GaInSb-on-InAs	3.2±0.2	301±39
(110)	InAs-on-GaInSb	1.9±0.1	112±16
(1$\bar{1}$0)	GaInSb-on-InAs	4.3±0.2	327±38
(1$\bar{1}$0)	InAs-on-GaInSb	2.8±0.2	174±21

Figure 16. Power spectral distributions for InAs-on-$Ga_{0.75}In_{0.25}Sb$ and $Ga_{0.75}In_{0.25}Sb$-on-InAs interfaces imaged in the (a) (110) and (b) (1$\bar{1}$0) cross-sectional planes. Both experimental data (symbols) and Lorentzian fits (solid and dashed lines) to the experimentally observed spectra are shown. (c) Amplitudes (Δ) and correlation lengths (Λ) corresponding to the fitted Lorentzian spectra plotted in a and b.

$$A_q = \frac{2}{N}\sum_{n=0}^{N-1} a(nd)\mathrm{e}^{-iqd} \tag{9}$$

where $q = 2\pi n/L$, L is the length of the interface profile, and d is the spacing between data points along the interface. A random distribution of steps at the interface is expected to yield an exponential correlation in real space and a Lorentzian power spectral distribution[75]

$$|A_q|^2 = \frac{1}{L}\frac{2\Delta^2(\Lambda/2\pi)}{1+(q\Lambda/2\pi)^2} \tag{10}$$

where Δ is the roughness amplitude and Λ the correlation length. Power spectral distributions calculated for interface profiles extracted from cross-sectional STM images were found to be well described by the Lorentzian function of eq 10.

Figure 16 shows power spectral distributions calculated for interface profiles extracted from (110) and (1$\bar{1}$0) cross-sectional STM images of the InAs/$Ga_{0.75}In_{0.25}Sb$ superlattice structure. Also shown in the figure are Lorentzian distributions fitted to the experimental data. The results shown in the figure incorporate analyses of several dozen interface profiles extracted from several images of both (110) and (1$\bar{1}$0) cross-sectional surfaces. Separate distributions were calculated for InAs-on-$Ga_{0.75}In_{0.25}Sb$ and $Ga_{0.75}In_{0.25}Sb$-on-InAs interfaces for each orientation, allowing the influence on interface structure of growth sequence as well as orientation to be determined. As indicated in Figure 16c, interfaces imaged in the (1$\bar{1}$0) cross-sectional plane were found to be significantly rougher, on average, than those imaged in the (110) plane. In addition, a substantial dependence of interface roughness on growth sequence was observed. For imaging in both the (110) and the (1$\bar{1}$0) cross-sectional planes, interfaces in which $Ga_{0.75}In_{0.25}Sb$ was grown on InAs were found to be significantly rougher than those in which InAs was grown on $Ga_{0.75}In_{0.25}Sb$.

The observation that interface roughness is greater in the (1$\bar{1}$0) plane than in the (110) plane is consistent with the formation on the epitaxially grown surface of islands elongated preferentially along the (1$\bar{1}$0) direction during epitaxial growth, a phenomenon that has been widely observed in planar studies of III−V epitaxial growth.[76−80] Islands or terraces elongated along the (1$\bar{1}$0) direction present on the surface during growth would be expected to produce corresponding features in epitaxially grown interfaces. Cross-sections of such interfaces would then exhibit greater roughness along the [110] direction, i.e., in the (1$\bar{1}$0) plane, than along the [1$\bar{1}$0] direction.

The dependence of interface roughness on growth sequence is consistent with the formation of interfaces with mixed stoichiometry for $Ga_{1-x}In_xSb$ grown on InAs. For infrared detectors based on InAs/$Ga_{1-x}In_xSb$ superlattices, it has been found that device characteristics may be optimized by deliberate growth of superlattice structures in which the InSb-like composition is present at both interfaces.[81] However, obtaining InSb-like composition at the $Ga_{1-x}In_xSb$-on-InAs interface requires that the As layer present on the InAs surface during growth by MBE be replaced by a layer of Sb prior to initiating deposition of $Ga_{1-x}In_xSb$. While studies by reflection high energy electron diffraction and X-ray photoelectron spectroscopy indicate that substantial substitution of Sb for As can be achieved by exposure of the As-terminated InAs surface to a pure Sb flux,[82,83] X-ray diffraction measurements indicate that only partial substitution of Sb for As occurs under typical growth conditions.[84] As shown schematically in Figure 17, the presence of mixed stoichiometry at a $Ga_{1-x}In_x$-Sb/InAs interface will inevitably lead to interface roughness, with the spectral distribution of roughness observed dependent upon the spatial distribution of Sb and As on the epitaxially grown surface and, consequently, at the heterojunction interface.

Additional insight into cross-incorporation of As and Sb in arsenide/antimonide heterostructures can be gained by examination of InAs/$InAs_{1-x}Sb_x$ heterostructures, in which the issue of interface abruptness is not complicated by the possible presence of multiple interface stoichiometries.[85] A cross-sectional STM image of an InAs/$InAs_{1-x}Sb_x$ superlattice grown by modulated molecular-beam epitaxy was shown in Figure 9. As indicated in Figure 18, the $InAs_{1-x}Sb_x$ layers grown by modulated MBE consisted of four-period 7.8 Å InAs/5.2 Å InSb superlattice structures. The resulting periodic structure within the $InAs_{1-x}Sb_x$

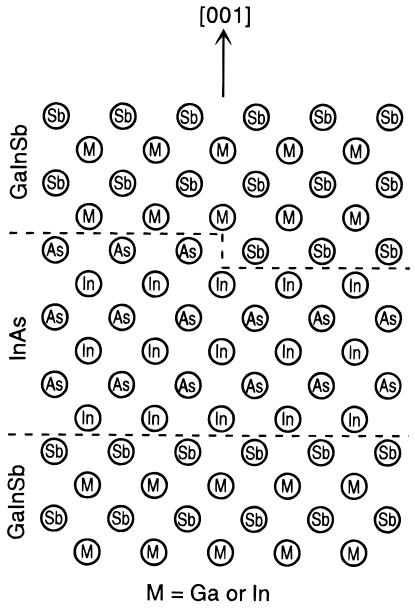

Figure 17. Schematic diagram of atomic layer structure for an InAs/$Ga_{1-x}In_xSb$ superlattice in which the stoichiometry is InSb-like at the InAs-on-$Ga_{1-x}In_xSb$ interface and has mixed InSb-like and $Ga_{1-x}In_xAs$-like character at the $Ga_{1-x}In_xSb$-on-InAs interface. The dashed lines delineate the interfaces between the layers. The presence of mixed stoichiometry at the $Ga_{1-x}In_xSb$-on-InAs interface can create additional interface roughness arising from the lateral inhomogeneity in composition.

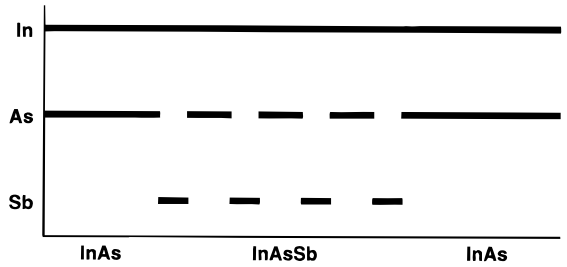

Figure 18. Schematic diagram of shutter sequence employed during growth of an InAs/$InAs_{1-x}Sb_x$ superlattice by modulated MBE. The lines indicate periods during which each shutter is open. In the modulated MBE growth technique, an InAs/InSb short-period superlattice is grown rather than a random $InAs_{1-x}Sb_x$ alloy. This approach has been demonstrated to yield higher structural quality and greater control over average alloy layer composition than can be achieved by solid-source MBE growth of a random group V alloy.

layer is clearly visible in Figure 9. The nominal average composition of the $InAs_{1-x}Sb_x$ layer is $InAs_{0.60}Sb_{0.40}$, based on the ratio of InAs to InSb layer thickness; X-ray diffraction measurements, however, yielded an average composition of $InAs_{0.76}Sb_{0.24}$, indicating the presence of substantial incorporation of As into the InSb-like layers.

Figure 19 shows a detailed, filled-state constant-current image of a single $InAs_{0.76}Sb_{0.24}$ layer within the InAs/$InAs_{0.76}Sb_{0.24}$ superlattice, obtained at a sample bias voltage of −2.4 V and a tunneling current of 0.1 nA. Several significant features may be noted in the image. The modulation in contrast arising from the modulated MBE growth technique is again clearly visible. However, substantial nanometer-scale lateral inhomogeneity is observed within the InSb-like layers, suggesting the presence of

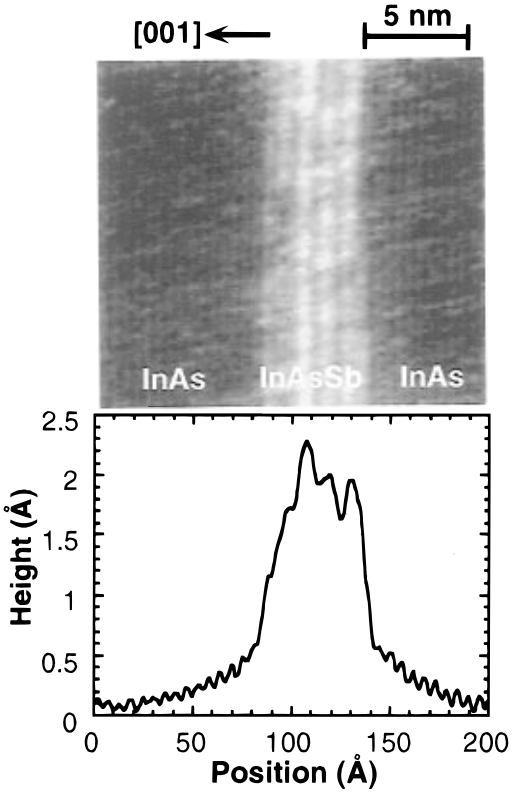

Figure 19. Filled-state cross-sectional STM image, obtained at a sample bias of −2.4 V and a tunneling current of 0.1 nA, of an $InAs_{0.76}Sb_{0.24}$ alloy layer grown by modulated MBE surrounded by InAs. An averaged topographic line scan is shown below the image. Modulation of the composition in the growth direction and nanoscale lateral inhomogeneity within the $InAs_{0.76}Sb_{0.24}$ alloy layer, along with a growth sequence dependence in interface abruptness, are visible in the image and the topographic profile.

compositional fluctuations arising from incorporation of As into the InSb-like layers. A dependence of interface abruptness on growth sequence is also visible in the image: the $InAs_{0.76}Sb_{0.24}$-on-InAs interface is seen to be atomically abrupt, while the InAs-on-$InAs_{0.76}Sb_{0.24}$ interface appears to suffer from compositional grading across one to two monolayers. Lew et al.[85] interpreted this grading to be evidence for Sb segregation at the growth surface during growth of the $InAs_{0.76}Sb_{0.24}$ layer followed by incorporation of Sb into the subsequently grown InAs layer, a phenomenon also found by Feenstra et al.[69−71] to occur during growth of InAs/GaSb superlattices by MBE. Finally, detailed examination of cross-sectional STM images of the InAs/$InAs_{0.76}Sb_{0.24}$ superlattice revealed that the average contrast, and by extension the average Sb content, increased from the first to third InSb-like layers within the $InAs_{0.76}Sb_{0.24}$ alloy, then decreased in the fourth and final InSb-like layer. This observation indicates that As incorporation into the InSb-like layers is most severe for the initially grown InSb-like layer, then gradually decreases. The reduced contrast observed in the final InSb-like layer is consistent with Sb segregation at the surface and incorporation into the subsequently grown InAs layer, and also suggests the occurrence of a slight amount of As diffusion into the underlying InSb-like layer.

e. Arsenide/Phosphide Heterostructures

Atomic-scale cross-incorporation and variations in interface composition are also significant issues for heterojunctions containing combinations of arsenide and phosphide compounds, e.g., InP/$In_{1-x}Ga_xAs$, InP/$In_{1-x}Ga_xAs_yP_{1-y}$, and GaAs/$In_{1-x}Ga_xP$. In cross-sectional scanning tunneling microscopy of InGaAs/InP multiple quantum well structures performed in air, topographic contrast between the InGaAs and InP layers was observed in constant-current images with corrugation amplitudes of up to 50−150 Å.[49,56,86] Cross-sectional STM studies of $In_{1-x}Ga_xAs$/InP multiple-quantum well structures under ultrahigh-vacuum by Osaka and Kato[87] yielded atomically resolved images of the $In_{1-x}Ga_xAs$ quantum-well layers; furthermore, the detailed contrast observed in constant-current images was found to vary with the dopant concentration in the sample: for positive bias voltages applied to the tip, the shape of the topographic profile reflected the shape of the valence-band-edge profile in the sample at a given dopant concentration. In addition, the corrugation amplitude measured as a function of bias voltage was used, in conjunction with theoretical modeling of the tunneling current, to estimate a valence-band offset $\Delta E_v = 0.60\Delta E_g$ between $In_{1-x}Ga_xAs$ and InP.

The detailed atomic-scale structure of alloy layers and heterojunction interfaces in various arsenide/phosphide heterostructures has been studied quite extensively by cross-sectional STM. In early studies of an InP/$In_{0.25}Ga_{0.75}As_{0.5}P_{0.5}$ heterojunction, Salemink and Albrektsen[88] obtained direct images of atomic-scale fluctuations in Group V composition in the quaternary alloy. In addition, recent studies of various arsenide/phosphide heterostructures by cross-sectional STM have revealed a considerable dependence of atomic-scale interface and alloy layer structure on growth conditions, with significant implications for the realization and optimization of arsenide/phosphide heterostructure devices. In cross-sectional STM studies of $In_{1-x}Ga_xAs$/InP double-barrier resonant-tunneling diodes grown by metalorganic MBE,[89,90] a dependence of both interface roughness and interface chemical composition on growth sequence was observed. As in the studies of interface roughness in InAs/GaSb[69−71] and InAs/$Ga_{1-x}In_xSb$[74] superlattices, interface profiles were extracted from constant-current images of the $In_{1-x}Ga_xAs$/InP resonant-tunneling-diode structure, and spatial frequency spectra were computed from these profiles. Fitting of the resulting spectra to a Lorentzian spectral distribution function revealed that the interfaces in which InP was grown on $In_{1-x}Ga_xAs$ were characterized by significantly shorter correlation lengths and larger roughness amplitudes than the $In_{1-x}Ga_xAs$-on-InP interfaces. In addition, constant-current images of the double-barrier regions revealed a growth-sequence-dependent asymmetry in the interfacial electronic structure which was believed to be a consequence of a difference in bonding types at the $In_{1-x}Ga_xAs$-on-InP and InP-on-$In_{1-x}Ga_xAs$ interfaces resulting from the growth procedures used.[89,90]

Lew et al.[91,92] have demonstrated that, under certain growth conditions, considerable atomic cross-incorporation and interfacial grading can occur at arsenide/phosphide heterojunction interfaces. Diffusion during growth interrupts was observed to be the most significant contributing factor, particularly as the growth temperature was increased. Figure 20 shows a schematic diagram and a filled-state cross-sectional STM image, obtained at a sample bias of −2.5 V and a tunneling current of 0.1 nA, of a structure in which growth of GaAs by gas-source MBE at a substrate temperature of 550 °C has been interrupted periodically and the surface exposed for 40 s to a pure P_2 flux. Growth interrupts and a variety of anion-switching procedures are often employed to optimize interface abruptness during growth of mixed arsenide/phosphide heterojunction interfaces. The filled (valence-band) states associated with P in the $GaAs_{1-x}P_x$ layers produced during the

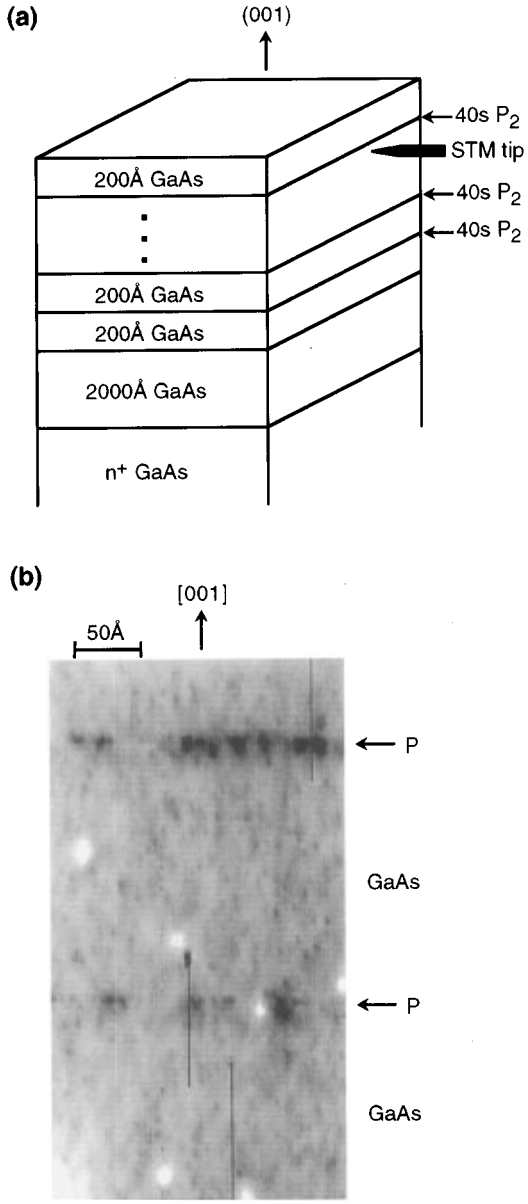

Figure 20. (a) GaAs/GaAsP heterostructure created by periodic exposure of a GaAs surface to a pure P_2 flux during growth by gas-source MBE. (b) Cross-sectional STM image of the structure shown in a, obtained at a sample bias of −2.5 V and tunneling current of 0.1 nA. The sample structure was grown at a substrate temperature of 550 °C. Topographic contrast indicated in the image reveals substantial incorporation of phosphorus into the GaAs during the exposure to P_2.

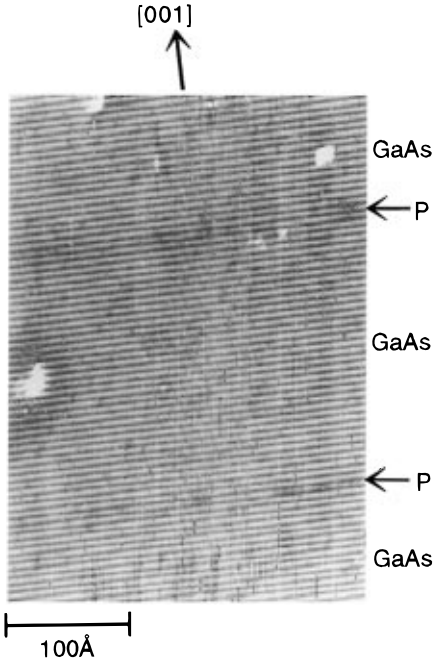

Figure 21. Cross-sectional STM image of a GaAs/GaAsP heterostructure nominally identical to that shown in Figure 20, but grown at a substrate temperature of 450 °C. The image was obtained at a sample bias of −2.5 V and a tunneling current of 0.1 nA. The contrast between the GaAs and GaAsP layers is extremely faint, indicating a much lower level of phosphorus incorporation than that present at higher growth temperatures.

growth interrupts are expected to have a lower energy than those associated with As;[93] the dark areas in the image therefore correspond to regions of phosphorus incorporation into the GaAs layers during the growth interrupts. Nanometer-scale lateral variations in phosphorus incorporation are clearly visible; furthermore, the contrast within the phosphide interlayers, averaged in the lateral direction, gradually increases in the [001] growth direction at the lower interface while decreasing more abruptly at the upper interface, suggesting that diffusion of phosphorus into the underlying GaAs is more significant than carryover of phosphorus into GaAs grown after the interrupt. Figure 21 shows a filled-state cross-sectional STM image of a nominally identical structure grown at 450 °C, obtained at a sample bias of −2.5 V and tunneling current of 0.1 nA. Comparison of the STM images of structures grown at 450 and 550 °C shows that the contrast associated with the $GaAs_{1-x}P_x$ layers formed during the growth interrupts, and consequently the amount of phosphorus incorporated during the interrupts, is dramatically reduced by growth at lower substrate temperatures, consistent with the interpretation that phosphorus incorporation occurs primarily via diffusion into the underlying GaAs.

Figure 22 shows a filled-state cross-sectional STM image, obtained at a sample bias of −2.5 V and a tunneling current of 0.1 nA, of a 67 Å $In_{1-x}Ga_xAs$/142 Å InP multiple-quantum-well structure grown by low-pressure organometallic vapor-phase epitaxy (OMVPE) at a substrate temperature of 650 °C.[92] The nominal composition of the ternary alloy layers, as determined by X-ray diffraction, is $In_{0.53}Ga_{0.47}As$; however, substantial variations in heterostructure

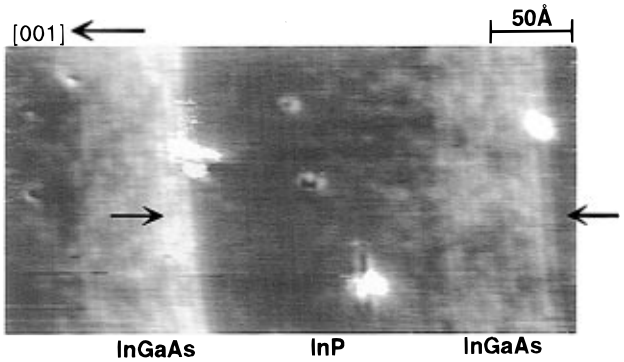

Figure 22. Filled-state cross-sectional STM image, obtained at sample bias voltage of −2.5 V and 0.1 nA tunneling current, of a 67 Å InGaAs/142 Å InP multiple-quantum-well structure grown by organometallic vapor-phase epitaxy. As incorporation in the InP layer near the InP-on-InGaAs interface is clearly visible. Contrast observed within the InGaAs layer suggests the occurrence of P diffusion into the InGaAs layer near the InP-on-InGaAs interface. Arrows indicate the region from which the topographic line profile shown in Figure 23 was extracted.

contrast, and by extension in composition and electronic structure, appear to be present within the $In_{0.53}Ga_{0.47}As$ layers. The $In_{1-x}Ga_xAs$ and InP layers appear bright and dark, respectively, consistent with the lower valence-band-edge energy in InP. Substantial contrast is observed in the InP layer near the InP-on-$In_{1-x}Ga_xAs$ interface, extending approximately 50−75 Å into the InP layer. Arsenic incorporation into InP layers grown on $In_{1-x}Ga_xAs$, arising from the presence of substantial residual As in the growth chamber, is believed to be a significant factor contributing to the contrast in the InP layer near the InP-on-$In_{1-x}Ga_xAs$ interface. Little such contrast is observed in the InP layer near the $In_{1-x}Ga_xAs$-on-InP interface. The heterojunction interface structure is thus clearly dependent on growth sequence, with the $In_{1-x}Ga_xAs$-on-InP interfaces appearing to be fairly abrupt and the InP-on-$In_{1-x}Ga_xAs$ interfaces exhibiting substantial interfacial grading. In addition, considerable inhomogeneity and a clear asymmetry in electronic structure in the direction of growth are visible in the $In_{1-x}Ga_xAs$ layer: the maximum contrast within the $In_{1-x}Ga_xAs$ layer relative to InP occurs near the $In_{1-x}Ga_xAs$-on-InP interface, with the contrast gradually decreasing in the growth direction. These features could arise from intermixing of either Group III or Group V constituents; however, the reduced contrast near the InP-on-$In_{1-x}Ga_xAs$ interface combined with the observation of phosphorus diffusion into GaAs during growth interrupts in gas-source MBE[91] suggests that phosphorus diffusion into the $In_{1-x}Ga_xAs$ layers during InP growth might contribute substantially to the observed asymmetry in samples grown by MOVPE.

This interpretation of the cross-sectional STM data is consistent with calculations of electrostatic band bending within an $In_{1-x}Ga_xAs$/InP heterostructure in which atomic cross-incorporation as described above has occurred.[94] Figure 23 shows the conduction-band-edge and valence-band-edge energies calculated for an $In_{1-x}Ga_xAs$/InP quantum-well structure in which cross-incorporation of As and P has occurred. Specifically, a self-consistent solution to Poisson's equation was obtained for a four-layer n-type ($n = 1$

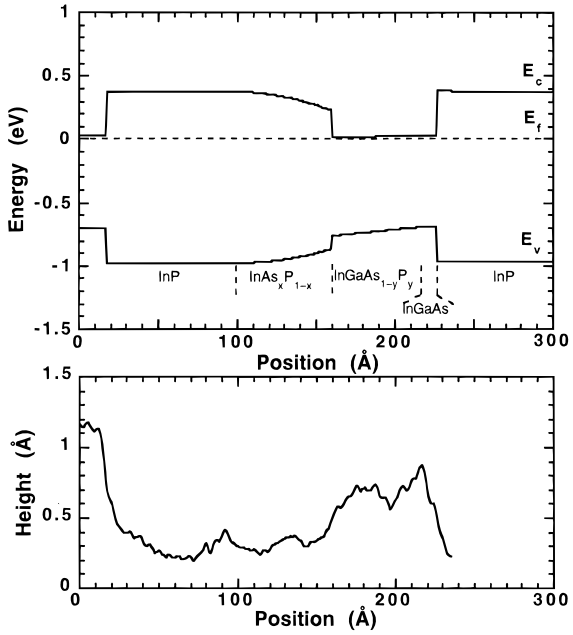

Figure 23. (a) Conduction-band-edge and valence-band-edge profiles calculated for an InGaAs/InP multiple quantum well structure in which As carryover into the InP layer and P diffusion into the InGaAs layer have occurred at the InP-on-InGaAs interface. (b) Topographic profile of the InGaAs/InP structure extracted from the filled-state image of Figure 22, obtained at −2.5 V sample bias. Nonuniform contrast within the quantum-well layer and evidence of As incorporation in the barrier layer near the InP-on-InGaAs interface can be seen in the topographic profile.

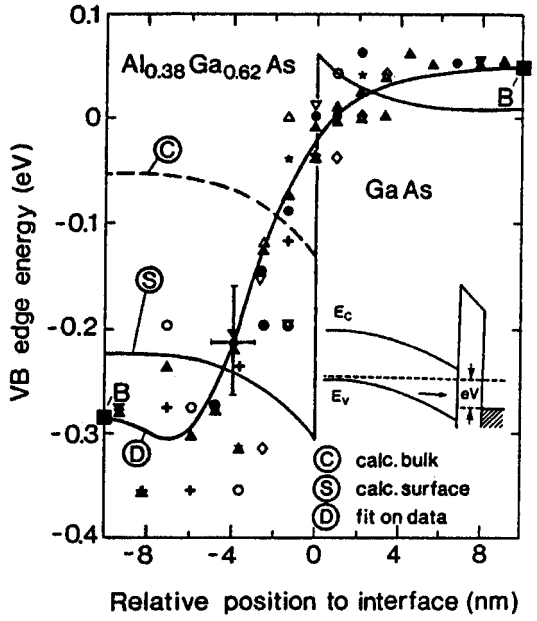

Figure 24. Valence-band-edge energies across a (110) crosssection of a GaAs/$Al_xGa_{1-x}As$ interface determined by scanning tunneling spectroscopy (symbols). The solid line (D) is a fit to the spectroscopic data. The dashed curve (C) is the calculated valence-band-edge profile for the heterojunction in bulk material, and the solid curve (S) is the calculated profile at the (110) surface, taking into account tip-induced band bending that occurs during the spectroscopic measurement. (Reprinted from ref 43. Copyright 1992 American Institute of Physics.)

$\times 10^{17}$ cm^{-3}) periodic structure with each period consisting of the following layers: (1) 82 Å InP; (2) 60 Å $InAs_xP_{1-x}$, with x increasing quadratically from 0 to 0.2; (3) 57 Å $InGaAs_xP_{1-x}$, with x increasing linearly from 0.9 to 1; and (4) 10 Å InGaAs. The individual layer widths in this structure were chosen to correspond approximately to the regions of different contrast observed in the cross-sectional STM image. Band-gap bowing parameters from the literature for the ternary and quaternary compounds were included when available;[95,96] otherwise values were obtained by linear interpolation between binary compounds. Valence-band offsets were assumed to vary linearly with composition, and the full effects of strain were included.[97] As seen in the figure, the band-edge profile calculated for a structure incorporating the effects of As carryover into InP and P diffusion into $In_{1-x}Ga_xAs$ at the InP-on-$In_{1-x}Ga_xAs$ interface is qualitatively consistent with the electronically induced contrast observed in the cross-sectional STM image of the InP/$In_{1-x}Ga_xAs$ multiple quantum-well structure grown by OMVPE.

f. Cross-Sectional Scanning Tunneling Spectroscopy

Detailed information regarding nanometer-scale electronic properties of semiconductor heterostructures can be obtained from cross-sectional scanning tunneling spectroscopy. Using scanning tunneling spectroscopy, Salemink et al.[41] were able to detect the two-dimensional electron gas formed at a GaAs/$Al_{0.5}Ga_{0.5}As$ interface with spatial resolution approaching 1 nm. In subsequent, detailed spectroscopic measurements on GaAs/$Al_xGa_{1-x}As$ heterojunctions,[42,43] the variation in valence-band-edge energy near the GaAs/$Al_xGa_{1-x}As$ interface was probed quantitatively with nanometer-scale resolution. Figure 24 shows valence-band-edge energies near a GaAs/$Al_xGa_{1-x}As$ interface determined using cross-sectional scanning tunneling spectroscopy; also shown are the valence-band-edge energy profile calculated in the vicinity of the interface in bulk material and at the (110) surface, the latter taking into account tip-induced band-bending in the sample that occurs during the spectroscopic measurement. A clear transition in the valence-band-edge energy, occurring over approximately 35−50 Å in the growth direction, is evident in the spectroscopic measurements. The distance over which the transition from the GaAs to the $Al_xGa_{1-x}As$ valence-band-edge energy occurred was taken to reflect the inherent width of the electronic transition across the heterojunction interface. The observed shift in valence-band-edge energy at the GaAs/$Al_xGa_{1-x}As$ interface is seen to be quantitatively consistent with the expected band offset for the heterojunction, provided that tip-induced electrostatic band bending in the sample is taken into account.

Detailed, quantitative interpretation of spectroscopic measurements on unpinned (110) surfaces of III−V semiconductors can be complicated considerably by tip-induced band-bending in the semiconductor, as described in section III. However, complications in quantitative interpretation of spectroscopic data arising from tip-induced band bending can to a limited extent be circumvented by performing spectroscopic measurements on surfaces for which the Fermi level is pinned. Such an approach is viable provided that the pinning does not completely ob-

scure the electronic properties of the bulk material. Gwo et al.[98] have explored this approach, performing imaging and spectroscopy on sulfide-passivated cross-sectional surfaces of GaAs/$Al_{0.3}Ga_{0.7}As$ heterostructures. Their experiments were interpreted as suggesting that the pinning induced by sulfide passivation did not alter the shift in valence-band-edge energy between the GaAs and $Al_{0.3}Ga_{0.7}As$ layers as measured by scanning tunneling spectroscopy, and that spectroscopic measurements were in fact able to probe the bulklike electronic properties of the sample. Pinnington et al.[99] have also used sulfur passivation of the cross-sectional surface to perform imaging and spectroscopy, in air, of GaAs/$Al_xGa_{1-x}As$ heterostructures and *pn* junctions. While these experiments demonstrate that sulfur passivation layers can facilitate certain types of spectroscopic measurements on (110) surfaces of III−V semiconductors, the ability to probe atomic-scale compositional structure and electronic properties is considerably reduced. Contrast between alternating layers in a heterostructure can generally be observed provided the layers are of sufficient thickness. However, atomic-scale details in the structure of alloy layers and heterojunction interfaces are generally obscured.

g. Profiling of Dopant Distributions

Characterization of dopant distributions and, indeed, of individual dopant atoms in III−V semiconductors has also been accomplished using cross-sectional STM. Muralt[38] performed the first cross-sectional studies of GaAs *pn* junctions, using scanning tunneling potentiometry to probe the potential distribution across a junction. Feenstra et al.[100] carried out the first detailed imaging and spectroscopic studies of GaAs *pn* junctions, observing electronically induced topographic contrast in which the *p*-type regions appeared to be ∼2 Å lower than the *n*-type regions for a sample bias voltage of −2 V. Also observed were unexpectedly large widths for the *n*-type layers compared to those expected from the growth procedure, and correspondingly smaller widths for the *p*-type regions; this was interpreted as evidence for diffusion of Si from the *n*-type layers into the surrounding *p*-type regions. Current-voltage spectroscopy allowed the *n*-type, *p*-type, and depleted regions to be identified unambiguously, confirming the interpretation of contrast in the constant-current images. Images and spectroscopic measurements consistent with these results were obtained in studies of GaAs *pn* junctions by Gwo et al.[101] Measurements of tunneling conductivity have been used by Feenstra et al.[102,103] to facilitate the study of *pn* junctions on cross-sectional surfaces containing relatively high densities of monoatomic steps. In constant-current STM imaging of these surfaces, the electronically induced topographic contrast between *p*-type and *n*-type regions is most likely diminished by partial pinning of the Fermi level,[102] and further obscured by actual topographic features on the stepped surface. Tunneling conductivity, however, was observed to vary with carrier type, allowing *p*-type, *n*-type, and depleted regions to be distinguished. In measurements of tunneling conductivity, the distance over which the transition in conductivity from the *p*-type to the *n*-type value occurred was found to be close to the expected depletion layer width for the junction, thereby providing a direct measure of the depletion length and, consequently, the dopant concentration.

Pinnington et al.[99] and Tseng et al.[104] have performed imaging and spectroscopy on GaAs *pn* junctions in air, using sulfide passivation to prevent oxidation of the cross-sectional surface. In both cases, electronically induced topographic contrast was observed between the *n*-type and *p*-type regions, with the *p*-type regions appearing 4−8 Å lower than the *n*-type regions for approximately −4 V bias applied to the sample; this degree of topographic contrast is comparable to that observed for sulfur-passivated GaAs *pn* junctions studied by cross-sectional STM under ultrahigh-vacuum conditions.[98] In addition, Tseng et al. observed a discrepancy between the apparent widths of the *p*-type and *n*-type regions in cross-sectional images and the layer widths expected from the growth procedure, with the *n*-type regions being substantially wider and the *p*-type regions narrower than intended. This was attributed to a shift in the apparent position of the *pn* junction arising from tip-induced band bending effects, rather than diffusion of Si from the *n*-type material into the adjacent *p*-type regions as postulated by Feenstra et al.[100] However, Gwo et al.[101] observed that the Fermi level on sulfur-passivated cross-sectional surfaces appeared to be pinned, which would tend to minimize tip-induced band-bending effects. While further work is required to understand fully the relative influence of actual sample structure and factors such as surface preparation, tip quality, and tip-induced band bending, it is clear that cross-sectional imaging and spectroscopic measurements with the STM offer the possibility of performing dopant profiling with a spatial resolution approaching 1nm, far better than the resolution achievable with more traditional characterization techniques.

h. Individual Dopant Atoms and Defects

In addition to nanometer-scale profiling of dopant distributions, cross-sectional STM has been used to study the properties of individual dopant atoms, defects, and other atomic-scale structures in GaAs. It has been demonstrated in high-resolution imaging of cleaved (110) surfaces of GaAs that Be and Zn dopant atoms in GaAs up to four layers below the cross-sectional surface can be detected, appearing as small hillocks in filled-state images of the cross-sectional surface; from the size and shape of the features, dopants at the surface and one layer below the surface could be distinguished from each other and from dopants farther below the surface.[105,106] The appearance of these hillocks was consistent with that expected on the basis of theoretical modeling of the effect of a Coulomb potential on the tunneling current. Figure 25 shows a constant-current cross-sectional STM image of a Be-doped GaAs sample. Individual dopant atoms, labeled 1−9, appear as "hillocks" in the image; the features labeled "a" and "b" were interpreted as As vacancies and adatoms, respectively. Detection of dopants in this manner was used to obtain dopant profiles in modulation-doped and δ-doped GaAs/AlGaAs epilayers.[107,108]

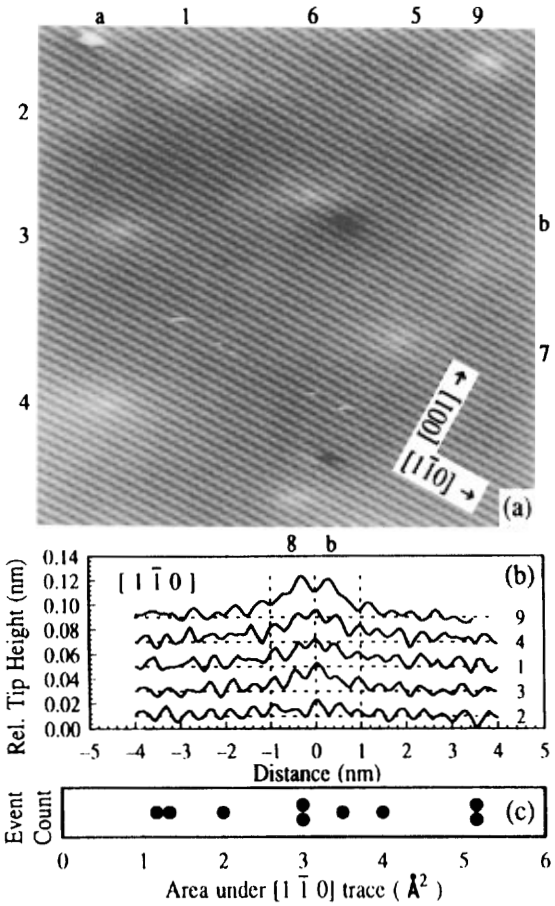

Figure 25. (a) Cross-sectional STM image of a Be-doped GaAs sample, obtained at a sample voltage of −2.1 V and a tunneling current of 0.1 nA. Individual Be dopant atoms, labeled 1−9, appear as "hillocks" in the image. (b) Topographic line scans through individual hillocks in a. (c) Distribution of areas under topographic line scans for each hillock. Larger areas correspond to dopant atoms closer to the surface; it was estimated that dopants up to five monolayers (∼10 Å) below the surface produced visible features in the image. (Reprinted from refs 105 and 106. Copyright 1993 American Institute of Physics.)

Results consistent with these were reported by Zheng et al., who obtained images of both Si donors[109] and Zn acceptors[110] in GaAs using cross-sectional STM.

In addition to dopants, features such as As antisite defects[111] and As precipitates[112] in low-temperature-grown GaAs have been studied by cross-sectional STM. Figure 26 shows constant-current cross-sectional STM images of defects observed in low-temperature-grown GaAs, in which a high concentration of As-related point defects were expected to be present. The four images shown in the figure were interpreted as each corresponding to an individual As antisite defect located zero, one, two, or three atomic planes below the (110) surface for images A, B, C, and D, respectively. The extended nature of the contrast observed in the images was believed to be a consequence of the spatially extended tails of the As antisite wave function.

i. Nanometer-Scale Optical Characterization

Optical measurements such as photoluminescence can serve as highly sensitive probes of certain atomic- to nanometer-scale properties of semiconductor heterostructures. For example, photoluminescence measurements performed on quantum-well structures by Sakaki et al.[113,114] were able to provide information about atomic-scale interface roughness and layer width fluctuations in GaAs/$Al_xGa_{1-x}As$ heterostructures. However, these photoluminescence measurements were sensitive primarily to interface roughness and layer width fluctuations at lateral length scales comparable to the typical exciton size (assumed to be ∼250 Å for GaAs[114]). Furthermore, such measurements inevitably average such atomic-scale properties over much larger length scales, and provide only indirect, and typically incomplete, information about local optical properties and their dependence on atomic-scale structural and electronic properties of materials and devices. Scanning probe techniques have made possible the direct characterization of optical properties at or near the nanometer scale.

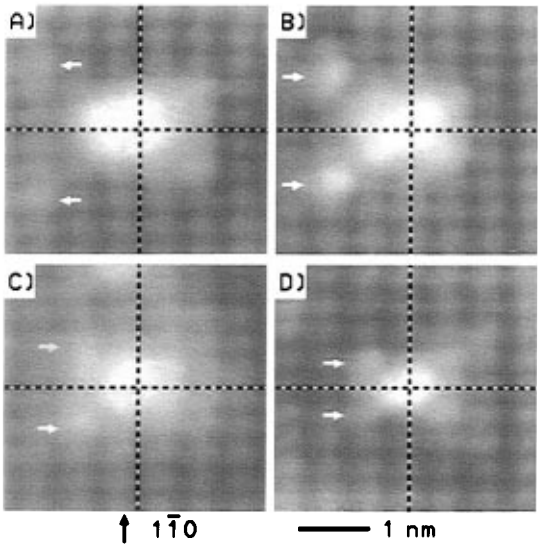

Figure 26. Constant-current STM images of defects observed in low-temperature-grown GaAs. Images A, B, C, and D were believed to correspond to As antisite defects located zero, one, two, or three atomic planes, respectively, below the (110) cross-sectional surface. (Reprinted from ref 111. Copyright 1993 American Institute of Physics.)

Detection of luminescence induced by recombination of carriers injected during imaging in a scanning tunneling microscope has allowed energy-band profiles and carrier transport characteristics in GaAs/$Al_xGa_{1-x}As$ quantum wells to be probed at the nanometer scale.[115−117] In these experiments, *p*-type GaAs/$Al_xGa_{1-x}As$ quantum-well structures were cleaved *in situ* in an ultrahigh-vacuum scanning tunneling microscope system. Light emission arising from recombination of electrons injected during constant-current imaging with holes present in the *p*-type material was measured, allowing luminescence properties to be probed with nanometer-scale spatial resolution. Higher luminescence intensity was observed while tunneling into the GaAs layers compared to that observed when injecting electrons into the $Al_xGa_{1-x}As$ layers, with the ratio of luminescence intensity in the different layers increasing for increasing magnitude of the bias voltage. Luminescence contrast from GaAs quantum wells as narrow as 20 Å was observed. For tunneling of electrons into both GaAs and $Al_xGa_{1-x}As$ layers, luminescence at photon energies corresponding to the

GaAs band gap was observed, suggesting that most of the injected electrons diffused to the GaAs quantum-well layers before recombining. Indeed, measurement of luminescence intensity as a function of lateral tip distance from a GaAs quantum well was used to estimate the diffusion length in $Al_xGa_{1-x}As$, and the value obtained was found to be in reasonable agreement with previously reported values. Detailed examination of the dependence of luminescence intensity on bias voltage revealed that the onset of luminescence occurred at bias voltages for which the tip Fermi level was just above the lowest energy conduction-band state in the sample; this contributed to a substantial difference at low to moderate bias voltages between luminescence intensity for electron injection into GaAs and that for electron injection into $Al_xGa_{1-x}As$. This difference was, as expected, consistent with contrast observed in luminescence imaging of the GaAs/$Al_xGa_{1-x}As$ quantum-well structures. A mapping of the threshold voltage for the onset of luminescence as the STM tip was scanned across a GaAs/$Al_xGa_{1-x}As$ multiple-quantum-well structure was found to correspond to the profile of the conduction-band-edge energy in the barrier regions, and of the lowest confined-state energy in the quantum wells, with energy variations observable at the nanometer scale.[117]

Given the eminent suitability of III−V semiconductors for characterization by cross-sectional STM and the increasing realization of the importance of atomic-scale material and device properties in heterostructure and nanoscale device technology, it is likely that cross-sectional STM studies of epitaxial layers and device structures will play a significant role in the development and application of advanced semiconductor heterostructures and nanostructures. Further development and effective utilization of this technique will require effort in a number of areas. A detailed understanding of the relationship between measured tunneling current (and, consequently, images and spectroscopic data) and the actual atomic-scale structure of the sample, including aspects such as local alloy-layer composition, ordering effects, interface stoichiometry, defects, and impurities, is essential; theoretical simulations of tunneling experiments are likely to be particularly useful. In addition, systematic comparisons of cross-sectional STM studies with data from various other characterization techniques such as transmission electron microscopy, X-ray diffraction, diagnostics such as RHEED performed during epitaxial growth, and optical and electrical measurements on a wide range of actual device structures will aid in the interpretation of STM data and ensure that high-resolution measurements performed on relatively small areas of a device do indeed provide information representative of the entire device structure.

V. Group IV Semiconductor Characterization

The overwhelming importance of Si in microelectronics technology provides a powerful motivation for applying scanning tunneling microscopy—in both the planar and cross-sectional geometries—to the characterization of Si and Si-based materials. Extensive studies using STM have been performed of fundamental properties of various Si surfaces and of processes such as epitaxial growth, adsorption of atoms and molecules, and etching on Si surfaces. Cross-sectional STM studies of epitaxial and device structures have been more limited, largely because preparation of a cross-sectional surface suitable for study by STM is much more difficult for Si than for III−V semiconductors: first, Si (001) wafers are more difficult to cleave than III−V wafers, although with some care flat (110) cleaved surfaces can be obtained; and second, the as-cleaved (110) cross-sectional surface has been found to be atomically disordered with electronic structure dominated by dangling-bond states.[118] Despite these complications, nanometer-scale cross-sectional characterization of Si-based materials and devices has been achieved. Detailed atomic-scale studies of such structures will, however, require the ability to prepare cross-sectional surfaces comparable in quality to cleaved (110) surfaces of III−V compounds.

a. Group IV Epitaxial Structures

Detailed cross-sectional imaging and spectroscopy of semiconductor materials and device structures requires, ideally, the production of an atomically flat, electronically unpinned surface. For III−V compounds, this is readily achieved by cleaving *in vacuo*. As mentioned above, however, cleaving of Si (001) wafers to obtain atomically flat (110) cross-sectional surfaces is highly problematic. Furthermore, the as-cleaved Si (110) surface tends to be disordered, and the Si (110) surface can exhibit a highly complex surface reconstruction. Nevertheless, Johnson and Halbout[119] have shown that an *ex situ* cleave of a Si (001) wafer followed by immersion in dilute HF can yield a (110) cross-sectional surface that is nearly atomically flat and is electronically unpinned. Using this sample preparation procedure, Yu et al. have performed electronic profiling of epitaxially grown Si *pn* junctions,[120] imaging and spectroscopy of Si/$Si_{1-x}Ge_x$ superlattices,[121] and two-dimensional electronic profiling of Si MOSFET structures.[122] Spatially resolved spectroscopic measurements obtained on cross sections of *pn* junctions grown by MBE revealed systematic variations in current−voltage spectra as the junction region was traversed; an analysis of these variations allowed the potential distribution in the junctions to be mapped out with spatial resolution on the order of 10 nm. In addition, changes in the potential distribution across the *pn* junction occurring as a reverse bias voltage was applied across the junction could be detected using potentiometric techniques. Spectroscopic techniques applied by Yu et al.[122] have been demonstrated to yield two-dimensional profiles of carrier type in Si MOSFET structures with spatial resolution on the order of 10−20 nm.

Cross sectional STM imaging of Si-based heterostructures has yielded results qualitatively similar to those obtained in studies of III−V heterostructures, but with reduced spatial resolution and sensitivity to local electronic structure because of the lower quality of the Si (110) cross-sectional surface. Electronically induced contrast between Si and $Si_{1-x}Ge_x$ layers similar to that seen in studies of

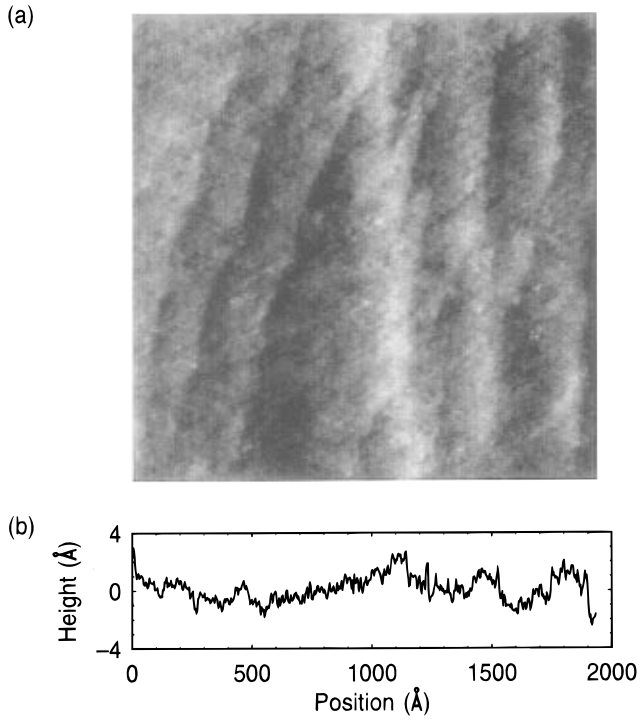

Figure 27. (a) (110) cross-sectional STM image of a 260 Å Si/75 Å $Si_{0.76}Ge_{0.24}$ strained-layer superlattice, near the interface between the superlattice and the underlying Si buffer layer. The growth direction is from left to right in the image. The image was obtained at a sample bias of +1.5 V and tunneling current of 0.1 nA. The bright regions correspond to the $Si_{0.76}Ge_{0.24}$ layers, and the dark to Si. Monolayer roughness of the surface is also visible in the image. (b) Line scan across the superlattice; the $Si_{0.76}Ge_{0.24}$ layers appear as peaks in the topography. (Reprinted from ref 121. Copyright 1992 American Institute of Physics.)

III−V heterostructures has been observed in constant-current cross-sectional images obtained under ultra-high-vacuum conditions of $Si/Si_{1-x}Ge_x$ superlattices[121] cleaved and passivated *ex situ*, and in images of passivated Si/Ge multilayers obtained in air.[123] Figure 27 shows a (110) cross-sectional STM image of a 260 Å Si/75 Å $Si_{0.76}Ge_{0.24}$ (001) strained-layer superlattice, obtained at a sample voltage of +1.5 V and a tunneling current of 0.1 nA.[121] The (110) cross-sectional surface was obtained using an *ex situ* cleave followed by immersion in a dilute HF solution as described above. The $Si_{0.76}Ge_{0.24}$ layers appear as bright vertical stripes in the image; three $Si_{0.76}Ge_{0.24}$ layers can be seen, with the underlying Si buffer layer visible in the left part of the image. Several monoatomic steps on the cleaved surface, running from the lower left to the upper right in the image, can also be seen. The presence of monolayer-level roughness on the (110) surface reduces the visibility in the gray-scale image of the electronically induced contrast between different materials in the superlattice, although the Si and $Si_{0.76}Ge_{0.24}$ layers can still be distinguished.

Figure 28 shows more detailed cross-sectional STM images of the $Si/Si_{0.76}Ge_{0.24}$ superlattice obtained at 0.1 nA tunneling current and sample bias voltages of (a) −2.5 V (filled-state) and (b) +1.8 V (empty-state). The characteristic shape of the superlattice corrugation is clearly different for images obtained at positive and negative sample bias, confirming that

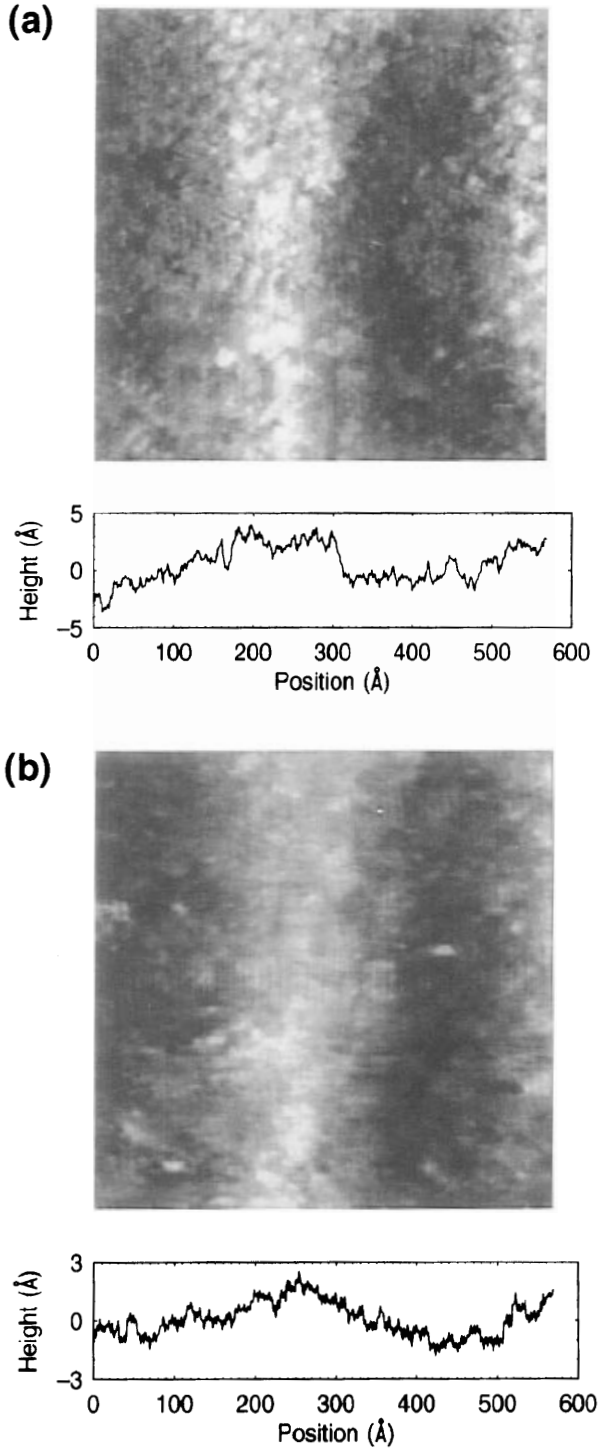

Figure 28. A (110) cross-sectional STM image of a 260 Å Si/75 Å $Si_{0.76}Ge_{0.24}$ strained-layer superlattice at 0.1 nA tunneling current and sample bias voltages of (a) −2.5 V and (b) +1.8 V. Below each image are single topographic line scans traversing the superlattice layers shown in each image. The growth direction in both images is from left to right.

the contrast is indeed electronically induced.[124] Also visible in the figure is monolayer-level roughness of the cross-sectional surface induced by the cleaving and HF etching procedure. Such roughness is likely to induce partial pinning of the surface. However, the electronic properties of the bulk material are still discernible in tunneling spectroscopy measurements, as evidenced by the spectroscopic studies of *pn* junctions described in refs 120 and 122. Indeed,

current−voltage spectra obtained for sequences of points traversing multiple periods of the $Si/Si_{1-x}Ge_x$ superlattice appeared to reflect nanometer-scale spatial variations in the electronic structure of the superlattice.[121]

Alternate methods for obtaining high-quality Si (110) cross-sectional surfaces have also been explored. Lutz et al.[118] have performed detailed studies of (110) surfaces cleaved and hydrogen passivated under ultrahigh-vacuum conditions, and have compared measurements from these surfaces to those obtained from samples cleaved *ex situ* and hydrogen passived by dipping in HF. Imaging and spectroscopy of (110) surfaces obtained by *in situ* cleaving revealed that the as-cleaved surface is disordered, with dangling-bond states in the band gap; substantial variations in local electronic structure were evident from spectroscopic measurements performed on as-cleaved surfaces. Upon exposure to atomic hydrogen, mostly passivated (110) surfaces were obtained, although completely homogeneous passivation of the entire surface was not observed. Spectroscopic measurements on epitaxial *p*-type and *n*-type Si layers indicated that surfaces prepared in this manner were partially pinned; however, *p*-type and *n*-type material could clearly be distinguished. Compared to the *ex situ* cleave and HF passivation procedure, the *in situ* approach yielded somewhat less homogeneous passivation but offered the possibility of reduced contamination and consequently more stable tunneling characteristics.

A comparison of images and spectroscopic data obtained from (110) cross-sectional surfaces of Group IV and III−V semiconductor heterostructures makes evident the importance of surface quality in high-resolution cross-sectional scanning tunneling microscopy. The atomically flat, electronically unpinned (110) surfaces obtainable by *in situ* cleaving for III−V semiconductors allow structure and electronic properties to be probed with atomic resolution, as described in section IV. For Group IV semiconductors, resolution and sensitivity to bulk electronic properties are currently limited to the nanometer scale by roughness, contamination, or inhomogeneous passivation on the (110) cross-sectional surface. Improvements in cross-sectional surface quality might be achievable either using improved passivation techniques for cleaved (110) surfaces or by cleaving to expose a (111) cross-sectional surface, for which etching in buffered HF has been shown to yield atomically flat surfaces.[125] Such improvements would be particularly valuable for improving spatial resolution and sensitivity to electronic properties in cross-sectional STM studies of Group IV materials and devices.

b. Si Device Structures

As feature sizes in advanced Si microelectronic devices such as metal−oxide−silicon field-effect transistors (MOSFET's) enter the ultrasubmicron, and eventually the nanometer-scale, size regime, the ability to characterize and ultimately to control fabrication processes and the resulting structure of a device with nanometer-scale spatial resolution has become essential. Indeed, successful fabrication of ultrasubmicron Si MOSFET's with gate lengths approaching 0.1 μm (100nm) and below will require the ability to characterize dopant and carrier profiles in the source and drain junction regions of a MOSFET with vertical and lateral resolution approaching 10 nm or better. Nanometer-scale characterization of and control over the source and drain junction profiles in ultrasubmicron MOSFET structures are especially critical for low-voltage, low-power applications that are becoming of central importance in microelectronics. However, such information can be extremely difficult to obtain using traditional characterization techniques such as spreading resistance profiling and secondary ion mass spectrometry (SIMS); the vertical resolution required for effective junction profiling is approaching the limits of these techniques, and the lateral resolution that can be achieved is far from adequate for this application.

A number of particularly promising approaches to this problem based on various scanning probe microscopies have begun to be explored. In this section we describe studies in which scanning tunneling microscopy and spectroscopy performed in the cross-sectional geometry have been used to delineate the electronic structure of Si MOSFET's with extremely high spatial resolution. Related techniques such as scanning capacitance microscopy,[126−130] scanning resistance microscopy,[131−133] Kelvin probe force microscopy,[134−137] and other scanning probe techniques[138−140] have also been used for extensive high-resolution characterization of Si *pn* junctions in both the planar and cross-sectional geometries. As feature sizes in state-of-the-art commercial microelectronic devices such as Si MOSFET's continue to shrink, scanning probe techniques are likely to assume increased importance for performing the nanometer-scale electronic and structural characterization of device structures and fabrication processes that will be essential for reliable, reproducible, and uniform fabrication of large-scale circuits based on ultrasubmicron devices.

Kordic et al.[141,142] performed the first cross-sectional STM studies of Si *pn* junctions, using the scanning tunneling microscope to study cross sections of implanted junctions exposed by cleaving. Experiments were conducted in which sample cleaving and subsequent tunneling measurements were performed both in air[141] and under ultrahigh vacuum conditions.[142] In both cases tunneling measurements were peformed directly on cleaved (110) surfaces rather than on surfaces that had undergone hydrogen passivation by immersion in an HF solution. Although the as-cleaved (110) surfaces were most likely to have been electronically pinned, the *pn* junctions could be detected using potentiometric techniques. Samples were fabricated with separate electrical contacts to the *p*-type and *n*-type regions of the *pn* junctions, and tunneling currents were measured while forward or reverse bias voltages were applied across the *pn* junction (in addition to an overall bias voltage applied to the sample relative to the tip). Differences in tunneling current measured in *p*-type, depleted, and *n*-type regions for various bias voltages applied to the *pn* junctions then revealed the electronic structure of the biased junctions. For experiments performed

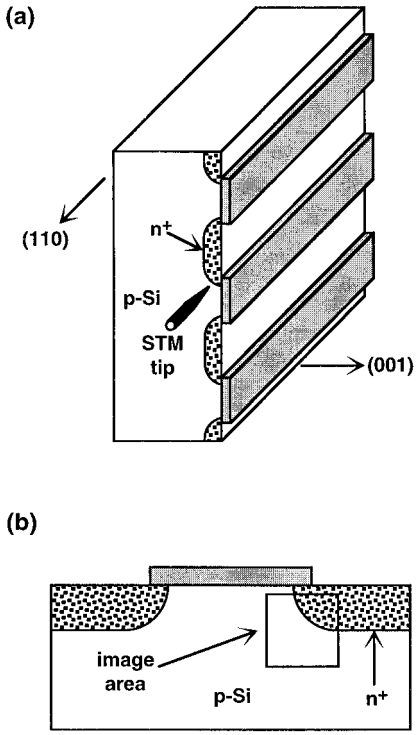

Figure 29. (a) Schematic diagram of the sample-tip geometry used for characterization of Si MOSFET structures by cross-sectional STM. (b) Location and orientation of topographic and current images.

under ultrahigh-vacuum conditions, the locations of the junctions could be resolved to within ~30 nm using these techniques.

Current imaging tunneling spectroscopy performed by Yu et al.[122] under ultrahigh-vacuum conditions on cleaved, hydrogen-passivated cross sections of Si metal−oxide−semiconductor (MOS) structures provided a demonstration of the ability, using cross-sectional STM, to characterize realistic device structures with spatial resolution in both the vertical and lateral directions on the order of ~10−20 nm. In this work, MOS structures were fabricated with gate and source/drain junction structure and topology characteristic of 0.1 μm Si MOSFET technology. The sample and tip geometry employed in these experiments is shown in Figure 29a. The geometry of the implanted junctions used in these studies was such that cleaving through regions containing multiple junctions and subsequently locating and imaging the junction regions was relatively straightforward.

Current imaging tunneling spectroscopy measurements were performed on the exposed cross sections of the MOS junctions as indicated in Figure 29b. Spatially resolved tunneling spectroscopy confirmed that clear differences were observable among current−voltage spectra obtained from *p*-type, *n*-type, and depleted regions of the junctions. Because the current−voltage spectra differed significantly for the *p*-type, *n*-type and depleted regions, current images generated from the spatially resolved tunneling current spectra were able to reveal the profiles of the *pn* junctions with extremely high spatial resolution in both the lateral and vertical directions.

Figure 30a shows a 160 nm × 160 nm constant-current topographic image of a junction region, obtained at a sample bias voltage of +1.5 V and a tunneling current of 1 nA. The location and orientation of the image region with respect to the junction structure are as indicated in Figure 29b; it is evident

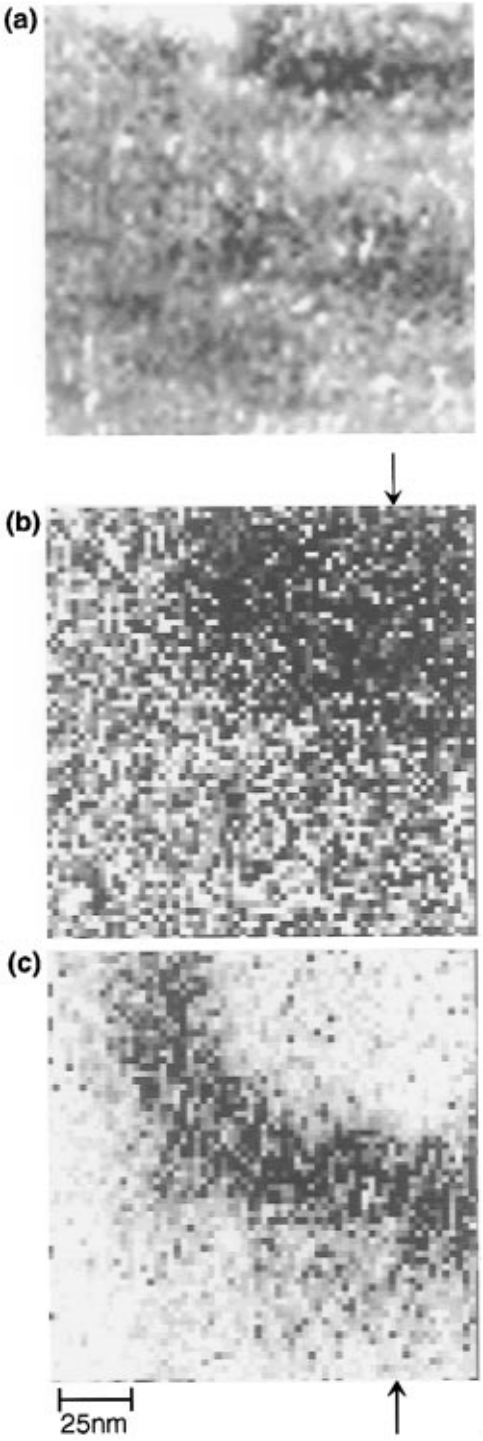

Figure 30. (a) A 160 nm × 160 nm constant-current topographic image of the junction region of a Si MOSFET, obtained at a sample bias of +1.5 V and a tunneling current of 1 nA. The gray-scale range is 0.5 nm. (b) Current image from the same area obtained for a sample bias of 2.0 V. The dark area, representing low tunneling current, corresponds to the n^+ source/drain region; the brighter area represents larger tunneling currents present in the *p*-type region. (c) Current image for a sample bias of −2.0 V. The dark band, representing large negative tunneling current, clearly delineates the depletion region of the junction; the brighter areas represent smaller negative tunneling currents present in the n^+- and *p*-type regions. (Reprinted from ref 122. Copyright 1996 American Institute of Physics.)

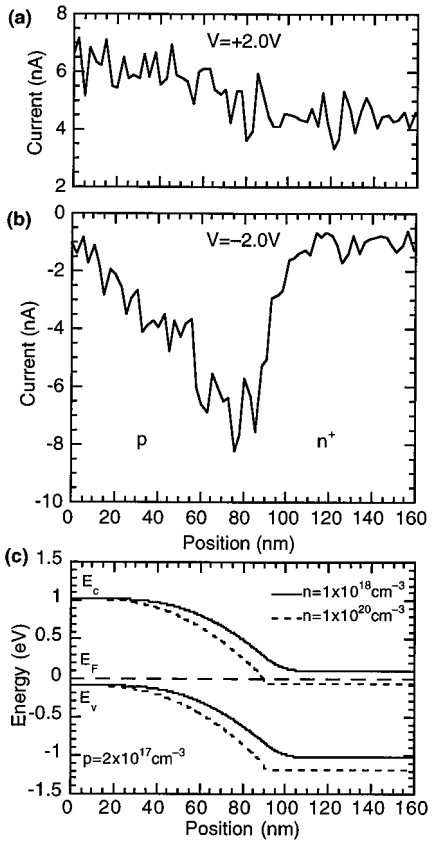

Figure 31. Tunneling currents measured along a line traversing the MOSFET junction as indicated by the arrows in Figure 30. Currents measured at sample bias voltages of (a) 2.0 V and (b) −2.0 V are shown. (c) Conduction- and valence-band-edge profiles calculated using dopant concentrations measured by SIMS. The region of increased negative tunneling current at negative sample bias corresponds to the depletion region of the *pn* junction.

from the figure that there is no clear correspondence between the topographic image and the electronic structure of the junction. Parts b and c of Figure 30 show current images from the same area obtained for sample bias voltages of +2 and −2 V, respectively, with the tip−sample separation at each point fixed by requiring a tunneling current of 1 nA to flow for +1.5 V sample bias voltage. In Figure 30b, the dark region corresponds to the small tunneling currents present in the n^+ source/drain region, while the brighter areas correspond to the larger positive tunneling currents measured in the *p*-type channel region. Intermediate values of the tunneling current are measured in the depletion layer, which therefore does not appear as a distinct region in the current image.

In contrast, one sees in Figure 30c that, for negative sample bias voltage, a small negative tunneling current is present in the n^+ source/drain region, and a somewhat larger negative current in the *p*-type region; most significantly, however, a dark band in the image, representing large negative tunneling currents present in the depletion layer, clearly delineates the shape of the junction. Figure 31 shows profiles of the tunneling currents measured at positive and negative sample bias along the line indicated by the arrows in Figure 30. For negative bias applied to the sample, a sharp increase in the magnitude of the tunneling current is seen at the edge of the n^+ region, providing a precise indication of the location of the *pn* junction to within ∼10−20 nm. The depletion layer width determined from tunneling spectroscopy measurements was found to agree well with that calculated using dopant concentrations obtained from SIMS measurements on the same samples, and the junction shapes seen in the current images were consistent with junction profiles obtained from transmission electron microscopy images of chemically delineated junctions.[122] The ability to perform two-dimensional carrier profiling of source and drain junctions in Si MOSFET's with spatial resolution on the order of 10 nm, as demonstrated in these experiments, will be a critical capability for successful realization and optimization of MOSFET circuits as gate lengths approach 0.1 μm and below.

VI. Summary and Conclusions

As the typical dimensions of advanced semiconductor devices approach the nanometer to atomic scale, the need to characterize, understand, and ultimately to control structure and electronic properties at or near the atomic scale is increasing. Cross sectional scanning tunneling microscopy has proven to be a powerful technique for probing the atomic to nanometer-scale properties of advanced semiconductor materials and device structures, providing valuable information about advanced compound semiconductor heterostructure materials and devices as well as ultrasubmicron Si microelectronic devices of relatively near-term commercial interest.

The utility of cross-sectional STM for performing characterization of semiconductor structures with extremely high spatial resolution is strongly dependent upon the ability to obtain cross-sectional surfaces that are uncontaminated, atomically flat, and electronically unpinned. For III−V semiconductors, such surfaces are achievable by cleaving under ultrahigh-vacuum conditions to expose (110) cross-sectional planes. Studies of III−V semiconductors by cross-sectional STM have, consequently, been extremely fruitful. Investigations of semiconductor heterojunctions in a variety of material systems have provided new information concerning atomic-scale structure of heterojunction interfaces—particularly for so-called mixed-anion material systems—and its dependence on epitaxial growth conditions. Detailed information concerning atomic-scale fluctuations in composition, clustering of atoms, and other such phenomena in ternary and quaternary III−V alloys has been revealed by cross-sectional STM; cross-sectional STM is particularly valuable in such studies by virtue of its sensitivity predominantly to local, atomic-scale composition and electronic properties at or extremely close to the cross-sectional surface. The spatial resolution afforded by STM has also made possible the characterization of individual dopant atoms and point defects in III−V semiconductors.

Studies of Group IV materials and device structures are of profound interest by virtue of the preeminence of Si in microelectronics technology. Cross sectional STM studies of Group IV semiconductor structures have been quite limited, however, due to the difficulty of obtaining a high-quality cross-sectional surface. Shortcomings in cross-sectional

surface quality also limit the lateral spatial resolution that can typically be achieved to the nanometer rather than atomic scale. Nevertheless, cross-sectional imaging of $Si/Si_{1-x}Ge_x$ heterostructures and carrier-type profiling of Si MOSFET structures with nanometer-scale resolution have been successfully achieved.

The application of scanning probe techniques generally, and cross-sectional STM in particular, to the characterization of advanced semiconductor materials and device structures is still in its early stages. A wide range of possibilities exists for further investigation of atomic-scale interface, alloy layer, and defect structure in a variety of III−V compound semiconductor material systems. Extensive studies of Group IV heterostructure materials and device structures would be enabled by improvements in techniques for preparing cross-sectional surfaces of Group IV semiconductors. In addition, STM and other scanning probe techniques have shown great promise and generated considerable interest for nanometer-scale characterization of ultrasubmicron Si electronic devices; continued advances in this area promise to have a significant impact on progress in advanced Si microelectronic technology.

Future work on cross-sectional STM is likely to benefit substantially not only from improvements in experimental techniques, e.g., for performing spectroscopy or for sample preparation, but also from increased use of detailed modeling and simulation to aid in the interpretation of images and spectroscopic data. As discussed in the previous sections, interpretation of images and especially quantitative interpretation of spectroscopic data can be complicated considerably by the fact that the atomic composition of the cross-sectional surface plane is often highly inhomogeneous and not completely known *a priori*. Theoretical modeling and simulation of tunneling currents are likely to help in providing a sound basis for interpretation of images and spectroscopic data obtained by cross-sectional STM.

In addition, it will be important to continue to investigate and establish correlations between results of atomic- to nanometer-scale characterization by cross-sectional STM and information about material and device properties obtained using other measurements that probe different material and device properties, that are sensitive to properties at larger length scales, or are otherwise complementary to cross-sectional STM. This is in fact of great importance for any characterization technique that provides information with extremely high spatial resolution but over a very small area or volume of the sample. For example, comparisons between atomic- to nanometer-scale characterization using cross-sectional STM and results of electrical transport measurements or optical measurements performed on actual device structures will provide information about the detailed relationship between atomic-scale properties and device behavior, and help confirm that information obtained from measurements over an extremely small area or volume are indeed representative of the whole.

Fabrication and characterization of nanometer-scale materials and devices have become, and promise to remain, pervasive themes of research in a wide range of fields. As scanning probe techniques generally and cross-sectional STM in particular are applied in an increasingly routine manner to a broad range of problems, they are likely to play a significant role in much of the progress that will be made in nanometer-scale science and technology. Work in this area promises to provide fertile ground for exploration and innovation in the coming years.

VII. Acknowledgments

Part of this work was supported by the National Science Foundation under Award nos. ECS 93-07986 and ECS 95-01469, and by an Alfred P. Sloan Research Fellowship.

VIII. References

(1) Binnig, G.; Rohrer, H. *Helv. Phys. Acta* **1982**, *55*, 726.
(2) Binnig, G.; Rohrer, H.; Gerber, Ch.; Weibel, E. *Appl. Phys. Lett.* **1982**, *40*, 178.
(3) Binnig, G.; Rohrer, H.; Gerber, Ch.; Weibel, E. *Phys. Rev. Lett.* **1982**, *49*, 57.
(4) Binnig, G.; Rohrer, H. *Surf. Sci.* **1983**, *126*, 236.
(5) Binnig, G.; Quate, C. F.; Gerber, Ch. *Phys. Rev. Lett.* **1986**, *56*, 930.
(6) Feenstra, R. M.; Stroscio, J. A.; Tersoff, J.; Fein, A. P. *Phys. Rev. Lett.* **1987**, *58*, 1192.
(7) Feenstra, R. M.; Stroscio, J. A. *J. Vac. Sci. Technol. B* **1987**, *5*, 923.
(8) Lutz, M. A.; Feenstra, R. M.; Chu, J. O. *Surf. Sci.* **1995**, *328*, 215.
(9) Van Loenen, E. J.; Dijkkamp, D.; Hoeven, A. J. *J. Microscopy* **1988**, *152*, 487.
(10) Dijkkamp, D.; Van Loenen, E. J.; Hoeven, A. J.; Dieleman, J. *J. Vac. Sci. Technol. A* **1990**, *8*, 218.
(11) Salemink, H.; Albrektsen, O. *J. Vac. Sci. Technol. B* **1991**, *9*, 779.
(12) Gomez-Rodriguez, J. M.; Baro, A. M.; Silveira, J. P.; Vazquez, M.; Gonzalez, Y.; Briones, F. *Appl. Phys. Lett.* **1990**, *56*, 36.
(13) Lew, A. Y.; Yu, E. T. Unpublished results.
(14) Hamers, R. J. *Annu. Rev. Phys. Chem.* **1989**, *40*, 531.
(15) Feenstra, R. M. *Surf. Sci.* **1994**, *299/300*, 965.
(16) Stroscio, J. A.; Feenstra, R. M. In *Scanning Tunneling Microscopy*; Stroscio, J. A., Kaiser, W. J., Eds.; Academic Press: San Diego, 1993; p 95.
(17) Feenstra, R. M.; Stroscio, J. A.; Fein, A. P. *Surf. Sci.* **1987**, *181*, 295.
(18) Hamers, R. J.; Avouris, Ph.; Bozso, F. *Phys. Rev. Lett.* **1987**, *59*, 2071.
(19) Feenstra, R. M.; Thompson, W. A.; Fein, A. P. *Phys. Rev. Lett.* **1986**, *56*, 608.
(20) Hamers, R. J.; Tromp, R. M.; Demuth, J. E. *Phys. Rev. Lett.* **1986**, *56*, 1972.
(21) Stroscio, J. A.; Feenstra, R. M.; Fein, A. P. *Phys. Rev. Lett.* **1986**, *57*, 2579.
(22) Tersoff, J.; Hamann, D. R. *Phys. Rev. Lett.* **1983**, *50*, 1998.
(23) Tersoff, J.; Hamann, D. R. *Phys. Rev. B* **1985**, *31*, 805.
(24) Bardeen, J. *Phys. Rev. Lett.* **1961**, *6*, 57.
(25) Selloni, A.; Carnevali, P.; Tosatti, E.; Chen, C. D. *Phys. Rev. B* **1985**, *31*, 2602.
(26) Lang, N. D. *Phys. Rev. B* **1986**, *34*, 5947.
(27) Bono, J.; Good, R. H., Jr. *Surf. Sci.* **1985**, *151*, 543.
(28) Bono, J.; Good, R. H., Jr. *Surf. Sci.* **1986**, *175*, 415.
(29) Mårtensson, P.; Feenstra, R. M. *Phys. Rev. B* **1989**, *39*, 7744.
(30) Feenstra, R. M. *Phys. Rev. B* **1995**, *50*, 4561.
(31) Stroscio, J. A.; Feenstra, R. M.; Fein, A. P. *J. Vac. Sci. Technol. A* **1987**, *5*, 838.
(32) Stroscio, J. A.; Feenstra, R. M.; Newns, D. M.; Fein, A. P. *J. Vac. Sci. Technol. A* **1988**, *6*, 499.
(33) Van Laar, J.; Huijser, A.; Van Rooy, T. L. *J. Vac. Sci. Technol.* **1977**, *14*, 894.
(34) Bechstedt, F.; Enderlein, R. *Semiconductor Surfaces and Interfaces*; Academie-Verlag: Berlin, 1988; Chapter 3.
(35) Gudat, W.; Eastman, D. E. *J. Vac. Sci. Technol.* **1976**, *13*, 831.
(36) Norman, D.; McGovern, I. T.; Norris, C. *Phys. Lett. A* **1977**, *63*, 384.
(37) Straub, D.; Skibowski, M.; Himpsel, F. J. *J. Vac. Sci. Technol. A* **1985**, *3*, 1484.
(38) Muralt, P. *Appl. Phys. Lett.* **1986**, *49*, 1441.
(39) Muralt, P.; Meier, H.; Pohl, D. W.; Salemink, H. W. M. *Appl. Phys. Lett.* **1987**, *50*, 1352.
(40) Muralt, P.; Pohl, D. W. *Appl. Phys. Lett.* **1986**, *48*, 514.

(41) Salemink, H. W. M.; Meier, H. P.; Ellialtioglu, R.; Gerritsen, J. W.; Muralt, P. R. M. *Appl. Phys. Lett.* **1989**, *54*, 1112.
(42) Albrektsen, O.; Arent, D. J.; Meier, H. P.; Salemink, H. W. M. *Appl. Phys. Lett.* **1990**, *57*, 31.
(43) Salemink, H. W. M.; Albrektsen, O.; Koenraad, P. *Phys. Rev. B* **1992**, *45*, 6946.
(44) Salemink, H. W. M.; Albrektsen, O. *J. Vac. Sci. Technol. B* **1992**, *10*, 1799.
(45) Albrektsen, O.; Meier, H. P.; Arent, D. J.; Salemink, H. W. M. *Appl. Phys. Lett.* **1993**, *62*, 2105.
(46) Zhang, Y.-H.; Chow, D. H. *Appl. Phys. Lett.* **1994**, *65*, 3239.
(47) Zhang, Y.-H. *Appl. Phys. Lett.* **1995**, *66*, 118.
(48) Reinhardt, F.; Dwir, B.; Kapon, E. *Appl. Phys. Lett.* **1996**, *68*, 3168.
(49) Kato, T.; Osaka, F.; Tanaka, I. *Jpn. J. Appl. Phys.* **1989**, *28*, 1050.
(50) Salemink, H.; Albrektsen, O. *Microelectron. Eng.* **1991**, *15*, 101.
(51) Vandenberg, J. M.; Panish, M. B.; Temkin, H.; Hamm, R. A. *Appl. Phys. Lett.* **1988**, *53*, 1920.
(52) Chang, J. C. P.; Chin, T. P.; Kavanagh, K. L.; Tu, C. W. *Appl. Phys. Lett.* **1991**, *58*, 1530.
(53) Ourmazd, A.; Tsang, W. T.; Rentschler, J. A.; Taylor, D. W. *Appl. Phys. Lett.* **1987**, *50*, 1417.
(54) Ourmazd, A.; Taylor, D. W.; Cunningham, J.; Tu, C. W. *Phys. Rev. Lett.* **1989**, *62*, 933.
(55) Ourmazd, A.; Baumann, F. H.; Bode, M.; Kim, Y. *Ultramicroscopy* **1990**, *34*, 237.
(56) Tanaka, I.; Kato, T.; Ohkouchi, S.; Osaka, F. *J. Vac. Sci. Technol. A* **1990**, *8*, 567.
(57) Gomez-Rodriguez, J. M.; Baro, A. M.; Silveira, J. P.; Vazquez, M.; Gonzalez, Y.; Briones, F. *Appl. Phys. Lett.* **1990**, *56*, 36.
(58) Albrektsen, O.; Arent, D. J.; Meier, H. P.; Salemink, H. W. *Appl. Phys. Lett.* **1990**, *57*, 31.
(59) Salemink, H. W. M.; Albrektsen, O. *J. Vac. Sci. Technol. B* **1992**, *10*, 1799.
(60) Johnson, M. B.; Maier, U.; Meier, H.-P.; Salemink, H. W. M. *Appl. Phys. Lett.* **1993**, *63*, 1273.
(61) Smith, A. R.; Gwo, S.; Sadra, K.; Shih, Y. C.; Streetman, B. G.; Shih, C. K. *J. Vac. Sci. Technol. B* **1994**, *12*, 2610.
(62) Smith, A. R.; Chao, K.-J.; Shih, C. K.; Shih, Y. C.; Streetman, B. G. *Appl. Phys. Lett.* **1995**, *66*, 478.
(63) Smith, A. R.; Chao, K.-J.; Shih, C. K.; Shih, Y. C.; Anselm, K. A.; Streetman, B. G. *J. Vac. Sci. Technol. B* **1995**, *13*, 1824.
(64) Zheng, J. F.; Walker, J. D.; Salmeron, M. B.; Weber, E. R. *Phys. Rev. Lett.* **1994**, *72*, 2414. Zheng, J. F.; Walker, J. D.; Salmeron, M. B.; Weber, E. R. *Phys. Rev. Lett.* **1994**, *73*, 368.
(65) Pfister, M.; Johnson, M. B.; Alvarado, S. F.; Salemink, H. W. M.; Marti, U.; Martin, D.; Morier-Genoud, F.; Reinhart, F. K. *Appl. Phys. Lett.* **1995**, *67*, 1459.
(66) Tuttle, G.; Kroemer, H.; English, J. H. *J. Appl. Phys.* **1990**, *67*, 3032.
(67) Brar, B.; Ibbetson, J.; Kroemer, H.; English, J. H. *Appl. Phys. Lett.* **1994**, *64*, 3392.
(68) Chow, D. H.; Miles, R. H.; Hunter, A. T. *J. Vac. Sci. Technol. B* **1992**, *10*, 888.
(69) Feenstra, R. M.; Collins, D. A.; Ting, D. Z.-Y.; Wang, M. W.; McGill, T. C. *Phys. Rev. Lett.* **1994**, *72*, 2749.
(70) Feenstra, R. M.; Collins, D. A.; Ting, D. Z.-Y.; Wang, M. W.; McGill, T. C. *J. Vac. Sci. Technol. B* **1994**, *12*, 2592.
(71) Feenstra, R. M.; Collins, D. A.; McGill, T. C. *Superlattices Microstruct.* **1994**, *15*, 215.
(72) Lew, A. Y.; Yu, E. T.; Chow, D. H.; Miles, R. H. *Appl. Phys. Lett.* **1994**, *65*, 201.
(73) Lew, A. Y.; Yu, E. T.; Chow, D. H.; Miles, R. H. *Mat. Res. Soc. Symp. Proc.* **1994**, *340*, 237.
(74) Lew, A. Y.; Zuo, S. L.; Yu, E. T.; Miles, R. H. *Appl. Phys. Lett.* **1997**, *70*, 75.
(75) Goodnick, S. M.; Ferry, D. K.; Wilmsen, C. W.; Liliental, Z.; Fathy, D.; Krivanek, O. *Phys. Rev. B* **1985**, *32*, 8171.
(76) Pashley, M. D.; Haberern, K. W.; Gaines, J. M. *Appl. Phys. Lett.* **1991**, *58*, 406.
(77) Sudijono, J.; Johnson, M. D.; Snyder, C. W.; Elowitz, M. B.; Orr, B. G. *Phys. Rev. Lett.* **1992**, *69*, 2811.
(78) Heller, E. J.; Lagally, M. G. *Appl. Phys. Lett.* **1992**, *60*, 2675.
(79) Pond, K.; Maboudian, R.; Bressler-Hill, V.; Leonard, D.; Wang, X.-S.; Self, K.; Weinberg, W. H.; Petroff, P. M. *J. Vac. Sci. Technol. B* **1993**, *11*, 1374.
(80) Tanimoto, M.; Osaka, J.; Takigami, T.; Hirono, S.; Kanisawa, K. *Ultramicroscopy* **1992**, *42*, 1275.
(81) Miles, R. H.; Schulman, J. N.; Chow, D. H.; McGill, T. C. *Semicond. Sci. Technol.* **1993**, *8*, S102.
(82) Wang, M. W.; Collins, D. A.; McGill, T. C.; Grant, R. W. *J. Vac. Sci. Technol. B* **1993**, *11*, 1418.
(83) Collins, D. A.; Wang, M. W.; Grant, R. W.; McGill, T. C. *J. Appl. Phys.* **1994**, *75*, 259.
(84) Miles, R. H.; Chow, D. H.; Hamilton, W. J. *J. Appl. Phys.* **1992**, *71*, 211.
(85) Lew, A. Y.; Yu, E. T.; Zhang, Y.-H. *J. Vac. Sci. Technol. B* **1996**, *14*, 2940.
(86) Osaka, F.; Tanaka, I.; Kato, T.; Katayama, Y. *Jpn. J. Appl. Phys.* **1988**, *27*, L1193.
(87) Osaka, F.; Kato, T. *J. Vac. Sci. Technol. B* **1993**, *11*, 1697.
(88) Salemink, H. W. M.; Albrektsen, O. *Phys. Rev. B* **1993**, *47*, 16044.
(89) Skala, S. L.; Wu, W.; Tucker, J. R.; Lyding, J. W.; Seabaugh, A.; Beam, E. A., III; Jovanovic, D. *J. Vac. Sci. Technol. B* **1995**, *13*, 660.
(90) Wu, W.; Skala, S. L.; Tucker, J. R.; Lyding, J. W.; Seabaugh, A.; Beam, E. A., III; Jovanovic, D. *J. Vac. Sci. Technol. A* **1995**, *13*, 602.
(91) Lew, A. Y.; Yan, C. H.; Tu, C. W.; Yu, E. T. *Appl. Phys. Lett.* **1995**, *67*, 932.
(92) Lew, A. Y.; Yan, C. H.; Welstand, R. B.; Zhu, J. T.; Tu, C. W.; Yu, E. T.; Yu, P. K. L. *J. Electron. Mater.* **1997**, in press.
(93) Harrison, W. A. *J. Vac. Sci. Technol.* **1977**, *14*, 1016.
(94) Lew, A. Y.; Yu, E. T. Unpublished results.
(95) Adachi, S. *Physical Properties of III-V Semiconductor Compounds*; J. Wiley and Sons: New York, 1992.
(96) Madelung, O., Ed. *Landolt-Börnstein: Numerical Data and Functional Relationships in Science and Technology*; Springer: New York, 1982; New Series III, Vol. 17. O. Madelung, ed., *Landolt-Börnstein: Numerical Data and Functional Relationships in Science and Technology*; Springer: New York, 1987; New Series III, Vol 22.
(97) Van de Walle, C. G. *Phys. Rev. B* **1989**, *39*, 1871.
(98) Gwo, S.; Chao, K. J.; Shih, C. K.; Sadra, K.; Streetman, B. G. *Phys. Rev. Lett.* **1993**, *71*, 1883.
(99) Pinnington, T.; Patitsas, S. N.; Lavoie, C.; Sanderson, A.; Tiedje, T. *J. Vac. Sci. Technol. B* **1993**, *11*, 908.
(100) Feenstra, R. M.; Yu, E. T.; Woodall, J. M.; Kirchner, P. D.; Lin, C. L.; Pettit, G. D. *Appl. Phys. Lett.* **1992**, *61*, 795.
(101) Gwo, S.; Smith, A. R.; Shih, C. K.; Sadra, K.; Streetman, B. G. *Appl. Phys. Lett.* **1992**, *61*, 1104.
(102) Feenstra, R. M.; Vaterlaus, A.; Yu, E. T.; Kirchner, P. D.; Lin, C. L.; Woodall, J. M.; Pettit, G. D. In Salemink, H. W. M., Pashley, M. D., Eds.; *Semiconductor Interfaces at the Sub-Nanometer Scale*; Kluwer Academic Publishers: Dordrecht, 1993; p. 127.
(103) Vaterlaus, A.; Feenstra, R. M.; Kirchner, P. D.; Woodall, J. M.; Pettit, G. D. *J. Vac. Sci. Technol. B* **1993**, *11*, 1502.
(104) Tseng, W. F.; Dagata, J. A.; Silver, R. M.; Fu, J.; Lowney, J. R. *J. Vac. Sci. Technol. B* **1994**, *12*, 373.
(105) Johnson, M. B.; Albrektsen, O.; Feenstra, R. M.; Salemink, H. W. M. *Appl. Phys. Lett.* **1993**, *63*, 2923.
(106) Johnson, M. B.; Albrektsen, O.; Feenstra, R. M.; Salemink, H. W. *Appl. Phys. Lett.* **1994**, *64*, 1454.
(107) Johnson, M. B.; Meier, H. P.; Salemink, H. W. M. *Appl. Phys. Lett.* **1993**, *63*, 3636.
(108) Johnson, M. B.; Koenraad, P. M.; van der Vleuten, W. C.; Salemink, H. W. M.; Wolter, J. H. *Phys. Rev. Lett.* **1995**, *75*, 1606.
(109) Zheng, J. F.; Liu, X.; Weber, E. R.; Ogletree, D. F.; Salmeron, M. *J. Vac. Sci. Technol. B* **1994**, *12*, 2104.
(110) Zheng, Z. F.; Salmeron, M. B.; Weber, E. R. *Appl. Phys. Lett.* **1994**, *64*, 1836.
(111) Feenstra, R. M.; Woodall, J. M.; Pettit, G. D. *Phys. Rev. Lett.* **1993**, *71*, 1176.
(112) Feenstra, R. M.; Vaterlaus, A.; Woodall, J. M.; Pettit, G. D. *Appl. Phys. Lett.* **1993**, *63*, 2528.
(113) Sakaki, H.; Tanaka, M.; Yoshino, J. *Jpn. J. Appl. Phys.* **1985**, *24*, L417.
(114) Tanaka, M.; Sakaki, H. *J. Cryst. Growth* **1987**, *81*, 153.
(115) Abraham, D. L.; Veider, A.; Schönenberger, Ch.; Meier, H. P.; Arent, D. J.; Alvarado, S. F. *Appl. Phys. Lett.* **1990**, *56*, 1564.
(116) Alvarado, S. F.; Renaud, Ph.; Abraham, D. L.; Schönenberger, Ch.; Arent, D. J.; Meier, H. P. *J. Vac. Sci. Technol. B* **1991**, *9*, 409.
(117) Renaud, Ph.; Alvarado, S. F. *Phys. Rev. B* **1991**, *44*, 6340.
(118) Lutz, M. A.; Feenstra, R. M.; Chu, J. O. *Surf. Sci.* **1995**, *328*, 215.
(119) Johnson, M. B.; Halbout, J.-M. *J. Vac. Sci. Technol. B* **1992**, *10*, 508.
(120) Yu, E. T.; Johnson, M. B.; Halbout, J.-M. *Appl. Phys. Lett.* **1992**, *61*, 201.
(121) Yu, E. T.; Halbout, J.-M.; Powell, A. R.; Iyer, S. S. *Appl. Phys. Lett.* **1992**, *61*, 3166.
(122) Yu, E. T.; Barmak, K.; Ronsheim, P.; Johnson, M. B.; McFarland, P.; Halbout, J.-M. *J. Appl. Phys.* **1996**, *79*, 2115.
(123) Pinnington, T.; Sanderson, A.; Tiedje, T.; Pearsall, T. P.; Kasper, E.; Presting, H. *Thin Solid Films* **1992**, *222*, 259.
(124) Yu, E. T.; Johnson, M. B.; Powell, A. R.; Halbout, J.-M.; Iyer, S. S. *J. Vac. Sci. Technol. B* **1993**, *11*, 1149.
(125) Higashi, G. S.; Becker, R. S.; Chabal, Y. J.; Becker, A. J. *Appl. Phys. Lett.* **1991**, *58*, 1656.
(126) Williams, C. C.; Slinkman, J.; Hough, W. P.; Wickramasinghe, H. K. *Appl. Phys. Lett.* **1989**, *55*, 1662.
(127) Williams, C. C.; Slinkman, J.; Hough, W. P.; Wickramasinghe, H. K. *J. Vac. Sci. Technol. A* **1990**, *8*, 895.
(128) Huang, Y.; Williams, C. C.; Slinkman, J. *Appl. Phys. Lett.* **1995**, *66*, 344.

(129) Huang, Y.; Williams, C. C.; Smith, H. *J. Vac. Sci. Technol. B* **1996**, *14*, 433.
(130) Neubauer, G.; Erickson, A.; Williams, C. C.; Kopanski, J. J.; Rodgers, M.; Adderton, D. *J. Vac. Sci. Technol. B* **1996**, *14*, 426.
(131) Shafai, C.; Thomson, D. J.; Simard-Normandin, M.; Mattiussi, G.; Scanlon, P. J. *Appl. Phys. Lett.* **1994**, *64*, 342.
(132) Shafai, C.; Thomson, D. J.; Simard-Normandin, M. *J. Vac. Sci. Technol. B* **1994**, *12*, 378.
(133) DeWolf, P.; Clarysse, T.; Vandervorst, W.; Snauwaert, J.; Hellemans, L. *J. Vac. Sci. Technol. B* **1996**, *14*, 380.
(134) Nonnenmacher, M.; O'Boyle, M.; Wickramasinghe, H. K. *Ultramicroscopy* **1992**, *42*−44, 268.
(135) Henning, A. K.; Hochwitz, T.; Slinkman, J.; Never, J.; Hoffman, S.; Kaszuba, P.; Daghlian, C. *J. Appl. Phys.* **1995**, *77*, 1888.
(136) Kikukawa, A.; Hosaka, S.; Imura, R. *Appl. Phys. Lett.* **1995**, *66*, 3510.
(137) Hochwitz, T.; Henning, A. K.; Levey, C.; Daghlian, C.; Slinkman, J.; Never, J.; Kaszuba, P.; Gluck, R.; Wells, R.; Pekarik, J.; Finch, R. *J. Vac. Sci. Technol. B* **1996**, *14*, 440.
(138) Abraham, D. W.; Williams, C.; Slinkman, J.; Wickramasinghe, H. K. *J. Vac. Sci. Technol. B* **1991**, *9*, 703.
(139) Weaver, J. M. R.; Wickramasinghe, H. K. *J. Vac. Sci. Technol. B* **1991**, *9*, 1562.
(140) Bourgoin, J.-P.; Johnson, M. B.; Michel, B. *Appl. Phys. Lett.* **1994**, *65*, 2045.
(141) Kordic, S.; Van Loenen, E. J.; Dijkkamp, D.; Hoeven A. J.; Moraal, H. K. *J. Vac. Sci. Technol. A* **1990**, *8*, 549.
(142) Kordic, S.; Van Loenen, E. J.; Walker, A. J. *Appl. Phys. Lett.* **1991**, *59*, 3154.

CR960084N